

REPORT DOCUMENTATION PAGE

Form Approved OMB No. 0704-0188

Public reporting burden for this collection of information is estimated to average 1 hour per response, including the time for reviewing instructions, searching existing data sources, gathering and maintaining the data needed, and completing and reviewing the collection of information. Send comments regarding this burden estimate or any other aspect of this collection of information, including suggestions for reducing the burden, to Department of Defense, Washington Headquarters Services, Directorate for Information Operations and Reports (0704-0188), 1215 Jefferson Davis Highway, Suite 1204, Arlington, VA 22202-4302. Respondents should be aware that notwithstanding any other provision of law, no person shall be subject to any penalty for failing to comply with a collection of information if it does not display a currently valid OMB control number.

PLEASE DO NOT RETURN YOUR FORM TO THE ABOVE ADDRESS.

1. REPORT DATE (DD-MM-YYYY)	2. REPORT TYPE Final Report	3. DATES COVERED (From – To) 30-Oct-09 - 30-Oct-10
------------------------------------	---------------------------------------	--

4. TITLE AND SUBTITLE Total Internal Reflection Ultrasonic Sensor for detection of subsurface flaws: proof of concept	5a. CONTRACT NUMBER STCU Registration No: P-367
	5b. GRANT NUMBER
	5c. PROGRAM ELEMENT NUMBER

6. AUTHOR(S) Professor Oleksandr (Alexander) V. Yurchenko	5d. PROJECT NUMBER
	5d. TASK NUMBER
	5e. WORK UNIT NUMBER

7. PERFORMING ORGANIZATION NAME(S) AND ADDRESS(ES) National Taras Shevchenko University of Kyiv 64, Volodymyrska street Kyiv 01033 Ukraine	8. PERFORMING ORGANIZATION REPORT NUMBER N/A
---	--

9. SPONSORING/MONITORING AGENCY NAME(S) AND ADDRESS(ES) EOARD Unit 4515 BOX 14 APO AE 09421	10. SPONSOR/MONITOR'S ACRONYM(S)
	11. SPONSOR/MONITOR'S REPORT NUMBER(S) STCU 08-8002

12. DISTRIBUTION/AVAILABILITY STATEMENT Approved for public release; distribution is unlimited.

13. SUPPLEMENTARY NOTES

14. ABSTRACT This report results from a contract tasking National Taras Shevchenko University of Kyiv as follows: The objective of the proposed study is to provide an experimental validation of the described concept. To achieve this objective it is necessary to solve two main tasks: (1) to analyze theoretically total internal reflection of an ultrasonic wave at a proper solid-solid interface and then to offer a sensor design based on the proposed technique; (2) to develop a test sample of the sensor, to fabricate it and examine its sensitivity to an artificial flaw in the tested object. Total internal reflection is observed only if velocity of the wave in the sensor body is less than velocity of the wave in the external medium (tested object). In optics, this condition is practically always satisfied because the reflecting interface is solid-air. In ultrasonics, this condition is easily satisfied in case of a liquid-solid interface because the sound wave velocity in liquids is much less than that in solids. In case of a solid-solid interface, the total internal reflection takes place if the sound velocity in the sensor body is less than that in the tested object. There are number of plastic materials with small sound velocities to be used but, as a rule, acoustic losses in these materials are great. (The best given values are ~2.5-3 dB/cm @ 5MHz. Moreover, there exist only a few materials with such relatively small losses; others have losses an order of magnitude greater). It makes them useless to build the TIRUS. At the same time, single crystal materials applied as a sensor body can provide extremely small sound velocity together with low acoustic loss. One of such materials is a monocrystal of paratellurite (tellurium dioxide) TeO2. In this crystal, the shear wave propagating along the [110] direction (δshear slow wave) has the velocity of 612 m/s and attenuation loss at 5 MHz as much low as 0.005 dB/cm. Using a prism of TeO2, total internal reflection can be achieved with a wide variety of tested materials at reasonable values of critical angles. Moreover, it can be used at much higher frequencies than plastics, up to 150 MHz. Accordingly, in practical applications a tested layer, whose thickness is of the order of the sound wavelength, can be much thinner. Because of very strong elastic anisotropy of the crystal, behavior of the shear slow wave in paratellurite is very specific. Directions of the phase and group velocities vectors can differ by tens of degrees. It results in very unusual reflection geometry to be taken into account. Necessary calculations based on the plane wave model will be done to find an appropriate sensor design. A test sample of the TIRUS will be fabricated and investigated. Expected results of the project accomplishment are as follows: calculation data on reflection of the slow shear ultrasonic wave at an arbitrarily oriented TeO2-solids interface; better understanding of total internal reflection of ultrasonic waves in strongly anisotropic medium; the developed design of the Total Internal Reflection Ultrasonic Sensor (TIRUS) using the TeO2 single crystal; results of experimental examination of the TIRUS.

15. SUBJECT TERMS

EOARD, Mechanical, Industrial, Civil And Marine Engineering., Structural Engineering and Building Technology

16. SECURITY CLASSIFICATION OF:			17. LIMITATION OF ABSTRACT UL	18, NUMBER OF PAGES 42	19a. NAME OF RESPONSIBLE PERSON SURYA SURAMPUDI
a. REPORT UNCLAS	b. ABSTRACT UNCLAS	c. THIS PAGE UNCLAS			19b. TELEPHONE NUMBER <i>(Include area code)</i> +44 (0)1895 616021

Standard Form 298 (Rev. 8/98)
Prescribed by ANSI Std. Z39-18

Project STCU P367-EOARD088002
Total Internal Reflection Ultrasonic Sensor for Detection of Subsurface Flaws:
Proof of Concept

FINAL TECHNICAL REPORT

Covering: Feb. 01, 2009 to Jan 31, 2010

Date of submission: March 31, 2010

Organization: National Taras Shevchenko University of Kyiv
64, Volodymyrs'ka St.,
01601 Kyiv, Ukraine

Project manager: Mr. Oleksandr Yurchenko
Senior Engineer
Department of Quantum Radiophysics
Tel.: +38 044 526-0572
email: alyur@univ.kiev.ua

Kyiv 2010

Project participants:

Dr. Leonid Ilchenko, Senior Research Associate

Dr. Sergiy Kolyenov, Assistant Professor

Mr. Iuriy Pilgun, Engineer

Mrs. Galyna Pogorielova, Senior Engineer

Dr. Eugene Smirnov, Associate Professor

Mr. Boris Tsurochka, Technician

Mr. Leonid Voitenko, Post Graduate Student

Mr. Mykola Yakovenko, Technician

CONTENTS

List of Symbols, Abbreviations and Acronyms	4
List of Figures.....	7
Summary.....	9
Introduction	9
1. Methods, Assumptions and Procedures	10
1.1 Concept.....	10
1.2 Theoretical background and substantiation of the calculation procedures.....	11
1.2.1 Propagation and reflection of plane elastic waves in TeO_2	11
1.2.2 The Fresnel zone of the emitting transducer and ultrasound beams in TeO_2	15
1.2.3 Simulation of ultrasonic beams propagation and reflections	17
2 Sensor design and fabrication	19
2.1 Choice of the sensor geometry.....	19
2.2 Sensor fabrication	20
3 Experimental studies of the sensor as a two-port network.....	22
3.1 Study with a continuous wave signal.....	22
3.2 Study with time-gated signals.....	26
4 Visualization of the sound beams in the sensor body	28
4.1 Experimental setup and technique	28
4.2 Identification of the sound field structure	29
5. Results and discussion	33
5.1 The sensor drawbacks.....	33
5.1.1 Mode conversions.....	33
5.1.2 Temperature instability	35
5.2 Results of the tested objects examination	36
5.2.1 Tested objects	36
5.2.2 Results of the continuous wave experiments	37
5.2.3 Results of the experiments with time-gated signals	38
Conclusions	39
Prospects.....	39
References	41

List of Symbols, Abbreviations and Acronyms

Acronyms

CW	continuous wave
DOUT	defective object under test
OUT	object under test
NDT	non-destructive testing
QL	quasi-longitudinal (elastic wave)
QSF	quasi-shear fast (elastic wave)
PM	pulse modulated
SSW	slow-shear wave
TIRUS	Total Internal Reflection Ultrasonic Sensor
VSWR	the voltage standing wave ratio

Symbols

Latin alphabet

a	a characteristic size of the transducer
AL	attenuation loss
A_{dB}	predetermined value in dB related to the maximum value of the ultrasonic field intensity on the reflecting plane of the TIRUS chosen to determine the ultrasonic beam boundaries
b	the anisotropy parameter
b_{110}	the anisotropy parameter along the [110] direction of TeO ₂
c_{ijkl} or $c_{\xi\xi}$	the stiffness tensor
D	distance between emitting and receiving transducers
DL	diffraction loss
f	frequency
I	the ultrasonic field intensity
I_{level}	the intensity level at which the ultrasonic beam boundaries are determined
I_{max}	the maximum value of ultrasonic intensity on the reflecting plane of the TIRUS
IL	insertion loss
\mathbf{K} and K_i	wave vector and its components
L	size of the emitting transducer along the [001] direction
L_{110}^0 and L_{001}^0	the path length passed by the ultrasonic wave in the TIRUS body along the [110] and [001] directions respectively at some initial temperature defined as "0"
L_{110}^T and L_{001}^T	the path length passed by the ultrasonic wave in the TIRUS body along the [110] and [001] directions respectively at some changed temperature defined as "T"
M_2	figure of merit of acousto-optic interaction
M_{2fq}	figure of merit related to that of fused quartz
m	the slowness (refraction) vector

\mathbf{m}^I and \mathbf{m}^R	the slowness vectors of the incident and reflected waves
m_{001} and m_{110}	magnitude of the slowness vectors along [001] and [110] directions
\mathbf{n} and n_i	the unit vector of the wave normal and its components
n	index of refraction
PL	propagation loss
P_{eff}	efficient photoelastic coefficient
p_{ijkl}	photoelastic tensor
RL	reflection loss
\mathfrak{R}	combined auxiliary factor in the efficient photoelastic coefficient introduced for simplicity of analysis
S_0	complex amplitude of the ultrasonic wave on the surface of the emitting transducer
T	complex transmission coefficient of the TIRUS
T_{TG}	transmission coefficient in the experiments with time-gated signals
TL	transduction loss
U_{in}	complex voltage at the TIRUS input in the continuous wave experiments
U_{out}	complex voltage at the TIRUS output in the continuous wave experiments
U_{pp_in}	measured peak-to-peak voltage at the TIRUS input in the time-gated experiments
U_{pp_out}	measured peak-to-peak voltage at the TIRUS output in the time-gated experiments
\mathbf{u} and u_i	the displacement vector and its components
u_i^I, u_i^R, u_i^T	components of the displacement vector of incident, reflected and transmitted waves
v	phase velocity of the elastic wave
v_{110}^0 and v_{001}^0	the ultrasonic wave velocity along the [110] and [001] directions respectively at some initial temperature defined as "0"
v_{110}^T and v_{001}^T	the ultrasonic wave velocity along the [110] and [001] directions respectively at some changed temperature defined as "T"
V_e	group (ray) velocity of the elastic wave
X_1, X_2, X_3	crystallographic coordinates
x, y, z	Descartes' coordinates tied to the transducer
y_0	the y-coordinate in the plane of the emitting transducer
y_{b1} and y_{b2}	the y-coordinate values on the reflecting plane determining the ultrasonic beam boundaries

Greek alphabet

$\boldsymbol{\alpha}$ and α_i	vector of polarization of the incident light wave and its components
α_j	thermal expansion coefficients along the crystallographic coordinates
α_{110}	thermal expansion coefficient along the [110] direction
$\boldsymbol{\beta}$ and β_i	vector of polarization of the diffracted light wave and its components
β	temperature coefficient of the efficient elastic constant
Γ_{il}	Christoffel's tensor
$\boldsymbol{\gamma}$ and γ_i	unit vector of the sound wave polarization and its components

γ	temperature coefficients of the sound wave velocities
γ_{110}	temperature coefficient of the SSW velocity along the [110] direction of TeO ₂
γ_{001}	temperature coefficient of the SSW velocity along the [001] direction of TeO ₂
$\Delta\varphi$	additional phase shift at the TIRUS output due to thermal effects
δ_{il}	the Kronecker delta
θ	a polar angle in spherical coordinates
θ_0	angle of incidence of the SSW ultrasonic wave
θ_K and θ_s	polar angles in spherical coordinates of the wave vector and of the group velocity (ray) vector
θ_h and θ_v	angles of deviation of the sensor body from the horizontal and the vertical in optical experiments
κ and κ_i	unit vector of the sound wave direction and its components
Λ	wavelength of sound
Λ_0	length of the sound wave propagating along the [110] direction
ρ	density of the material
ρ_{12}	correlation coefficient between two sets of data
σ	standard deviation
τ	delay time
φ	a polar angle in spherical coordinates
φ_{ij}	auxiliary tensor used in calculation of the efficient photoelastic coefficient
ϕ	phase of the TIRUS transmission coefficient
ω	cyclic frequency

List of Figures

Note: Figures are numbered continuously through the "one-dot (#.#)" sections of the report.

- 1.1.1. Configuration of the Total Internal Reflection Ultrasonic Sensor (TIRUS) with the TeO₂ prism.
- 1.2.1. Orientation of directions and planes of interest with respect to Descartes' and Spherical coordinates.
- 1.2.2. Reflection of the plane slow shear wave in plane (1 $\bar{1}$ 0) of TeO₂: the "purest case".
- 1.2.3. Reflection of the plane slow shear wave in plane (1 $\bar{1}$ 0) of TeO₂: an "odd case".
- 1.2.4. Polarization of the slow shear waves propagating in plane (1 $\bar{1}$ 0) of TeO₂.
- 1.2.5. The intensity field of an ultrasonic transducer emitting in the [110] direction of TeO₂.
- 1.2.6. Illustration of the heuristic procedure developed to determine boundaries of ultrasonic beams.
- 1.2.7. Distribution of the sound intensity across the reflecting plane.
- 1.2.8. Simulation of propagation and reflection of the slow shear wave beam in plane (1 $\bar{1}$ 0) of TeO₂.
- 2.1.1. The sensor body geometry providing the total internal reflection of the incident ultrasonic beam for a wide variety of tested materials.
- 2.1.2. The sensor body geometry accepted as suitable for fabrication of an experimental sample of the TIRUS.
- 2.2.1. The sensor body with bonded piezoelectric transducers.
- 2.2.2. The light diffraction pattern representing the sound field distribution in the (001) plane.
- 2.2.3. VSWR of the sensor input vs frequency.
- 2.2.4. VSWR of the sensor output vs frequency.
- 3.1.1. The ultimate construction of the Total Internal Reflection Ultrasonic Sensor (TIRUS).
- 3.1.2. A schematic of the measurement setup used in the continuous wave experiments.
- 3.1.3. The frequency response of the TIRUS with the receiving transducer located in a calculated position.
- 3.1.4. The frequency response of the TIRUS with the shifted receiving transducer.
- 3.1.5. Phenomenon of stationary points at the frequency response of the TIRUS.
- 3.1.6. Instability of the TIRUS frequency response.
- 3.1.7. Normalized FFT coefficients used in the continuous wave experiments as reference data.
- 3.2.1. A schematic of the measurement setup used in the experiments with time-gated signals.
- 3.2.2. A typical waveform acquired from the oscilloscope in the experiments with time-gated signals.
- 4.1.1. The sensor body orientation with respect to the optical system axes.
- 4.1.2. Appearance of the optical part of the experimental setup.
- 4.2.1. Diffraction pattern: the CW signal is applied.
- 4.2.2. Diffraction pattern: the PM signal is applied.
- 4.2.3. Diffraction pattern: no signal is applied.
- 4.2.4. Visualization of the SSW beam emitted by the transducer.
- 4.2.5. Visualization of the SSW beam emitted by the transducer – the processed image.
- 4.2.6. Observation of the Schaefer-Bergmann's diffraction pattern.
- 4.2.7. The calculated slowness surfaces of sound waves propagating in the (1 $\bar{1}$ 0) plane of TeO₂.
- 4.2.8. Superimposition of the diffraction patterns obtained in the small- and the large-aperture experiments.
- 4.2.9. Directions of the ray vectors of the observed wave derived from the directions of their wave vectors \mathbf{K} .

- 5.1.1. Multiple responses at the TIRUS output.
- 5.1.2. Estimation of the delay time of the slow shear wave propagating in the crystal.
- 5.1.3. Polarization of the divergent slow shear wave beam propagating in plane (001) of TeO₂.
- 5.1.4. Change of the TIRUS insertion phase in time in the continuous wave experiments.
- 5.2.1. An assembly "TIRUS-OUT" used in experiments with a defective Object Under Test.
- 5.2.2. Flawless specimens used in the experiments.
- 5.2.3. Defective specimens with a single defect.
- 5.2.4. Results of the continuous wave experiments with different tested specimens: comparison with the reference data.
- 5.2.5. Time-gated transmission coefficient of the TIRUS measured with different tested specimens.

Summary

The research carried out in the current project aimed at proof of feasibility of a proposed novel technique/sensor based on total internal reflection of ultrasonic bulk waves from the solid-solid interface. The entire study planned for the project is completed excluding investigations with a liquid couplant between contacting surfaces of the sensor and a tested object. This exclusion was made because some data obtained were equivocal and required additional time to sort them out and to get reliable conclusive results related to the Total Internal Reflection Ultrasonic Sensor (TIRUS) concept. Thus, all conclusions made are based on the results obtained from the experiments with specimens bonded to the sensitive face of the sensor using an optical contact technology. Propagation and reflection of the plane slow shear waves (SSW) in the $(1\bar{1}0)$ plane of the TeO_2 single crystal was studied and behavior of ultrasonic beams was simulated. As a result, a proper design of the sensor body was developed. Optical studies of the sound field structure revealed an unexpected conversion of the excited SSW into other types of waves, quasi-shear fast (QSF) and quasi-longitudinal (QL) ones. Investigation of the TIRUS as a two-port network with both the continuous wave and time-gated signals resulted in a convincing conclusion. A distinctive difference has been shown between the TIRUS responses to flawless and defective tested objects that proves feasibility of the proposed concept and the developed technique. It can be used as a basis for further fundamental investigations as well as for development of relevant devices.

Introduction

One of the common disadvantages listed in the recent assessment of the widespread ultrasonic NDT techniques is that [1, p.10] "Discontinuities that are in a thin layer immediately below the surface are difficult to detect". The current report represents the results of original experimental research on a novel ultrasonic technique/sensor, called here Total Internal Reflection Ultrasonic Sensor (TIRUS), aimed at detecting such discontinuities. The concept of such a technique is set out briefly in Section 1.1. What has been done in the course of the project, to which extent its purposes are achieved, and what should be done further is summed up in the "Conclusions" and "Prospects".

Although experimental investigations were the very essential part of the research, results of which could only provide proof-of-concept of the proposed technique, the need in designing of an experimental sample of the TIRUS required a theoretical base to make necessary calculations. The theory of plane elastic waves in crystals [2, 3] and a Huygens' principle applied to ultrasonic waves in uniaxially anisotropic media [4] were used as such one. For simplicity, only a very minimum of theoretical material is placed into the report necessary to understand the procedures put into the base of the simulating software developed to design the sensor. Section 1.2 represents this theoretical material and a heuristic procedure developed to simulate propagation and reflection of ultrasonic beams in the $(1\bar{1}0)$ plane of TeO_2 . Details of the calculation procedure implemented into the developed simulating software are described in Section 1.2.3. Application of this software to designing of the TIRUS body resulted in ultimate choice of the crystal geometry, which then was realized in the fabricated experimental sample of the TIRUS. This constitutes the content of Section 2.

In Section 3, experimental techniques are described applied to studying the TIRUS experimental sample as a two-port network. Significant instability of the TIRUS characteristic is discovered and approaches are proposed to avoidance of its destructive effect using both post-processing of data acquired and time-gated signals.

In Section 4, optical visualization of the sound field structure in the crystal reveals ultrasonic beams of quasi-shear fast and quasi-longitudinal waves whose presence is inexplicable in the frame of the plane elastic waves theory used as a base in all calculations made in the current project. In Section 5.1, the problems faced in investigations of TIRUS characteristics and the ways to overcome them are discussed.

Despite the revealed problems, data obtained in the two-port-network experiments with flawless and defective tested specimens show that the idea works. Crucial results proving the TIRUS concept are provided and discussed in Section 5.2.

1. Methods, Assumptions and Procedures

The reported experimental studies of the Total Internal Reflection Ultrasonic Sensor (TIRUS) were based on the premise that simple physics underlying some of the near-field techniques in optics could work in ultrasonics as well. The lack of any previous research on the subject made it unclear which specific experimental methods were most suitable to achieve the goal of the research, to prove feasibility of the TIRUS. Therefore, two different approaches had been planned and then realized in the course of the project. The one was to study the transfer function (insertion loss) of the TIRUS. Visualization of the sound beams in the sensor body was another. Both of them, as well as theoretical background and assumptions underlying the development of software necessary to design the sensor itself are described in this section. In the beginning, the concept of the TIRUS as it was represented in the proposal of this study is stated concisely.

1.1 Concept

The research carried out in this project has been aimed at proof of feasibility of a novel technique/sensor using *total internal reflection of ultrasonic bulk waves at the solid-solid interface*, a boundary between the sensor and the tested object.

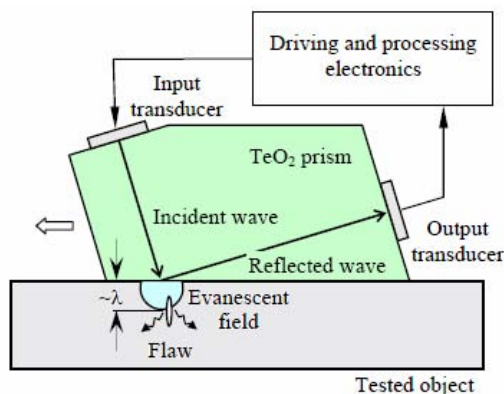


Fig. 1.1.1. Configuration of the proposed Total Internal Reflection Ultrasonic Sensor (TIRUS) with the TeO_2 prism.

According to the initial assumption, based on the simplest model describing propagation and reflection of plane elastic waves in the anisotropic medium, in this case, there are no refracted bulk waves in the tested object but there exists an evanescent field near its boundary. A sub-surface flaw/heterogeneity in the tested object is supposed to affect the evanescent field/wave excited by the wave *incident from a solid body of the sensor*. In its turn, the affected evanescent field disturbs the field of the wave reflected into the sensor body.

Change of the wave magnitude and/or phase can be used as an informative agent in the proposed NDT technique. As long as no refracted waves in the tested object exist, there are no factors affecting the reflected wave in the sensor body except the evanescent field. Thus, the

information signal is obtained only from the subsurface flaw under the “reflection footprint”. This idea is illustrated in Fig. 1.1.1.

The total internal reflection of the sound wave is impossible unless its velocity v in the sensor body is less than that in the tested object. For this reason, suitable materials for the sensor should be chosen among ones with small sound velocity and, evidently, small acoustic loss. A number of single crystal materials represent such properties. The sound velocity of the slow shear wave in one of them, paratellurite (TeO_2), is ~ 612 m/s, which therefore looks very suitable to be applied as an ultrasonic probe in the sensor body. The experimental study of such a sensor constitutes the subject of this project.

One additional important point should be mentioned here. When a flaw in the evanescent field under the “reflection footprint” is present, the total internal reflection will be frustrated and some unpredictable refracted waves will appear in the object under test. Even though these waves exist, their influence on the information component in the probing ultrasonic wave reflected from the interface can be excluded using time-gated signals.

1.2 Theoretical background and substantiation of the calculation procedures

1.2.1 Propagation and reflection of plane elastic waves in TeO_2

The theory of plane elastic waves in crystals is developed thoroughly. Its main results [2] related to propagation and reflection of bulk waves are as follows.

Generally, for a given direction of the wave normal \mathbf{n}^i of the elastic wave, its phase velocity v and the displacement vector \mathbf{u} are determined from the Christoffel's equation

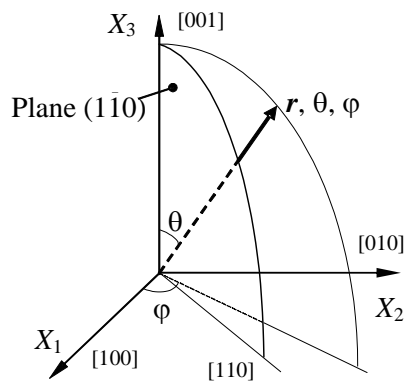


Fig. 1.2.1. Orientation of crystallographic directions and planes of interest with respect to Descartes' and Spherical coordinates.

$$\rho v^2 u_i = \Gamma_{il} u_l, \quad (1.2.1)$$

where ρ is the crystal density and the symmetrical second rank Christoffel tensor

$$\Gamma_{il} = c_{ijkl} n_j n_k. \quad (1.2.2)$$

Here c_{ijkl} is the fourth rank stiffness tensor, its indices i, j, k, l range from 1 to 3 and correspond to the Descartes' coordinate system presented in Fig. 1.2.1. In the same Figure the notation for the spherical coordinate system (r, θ, φ) and some crystallographic planes and directions are presented, which will be of specific interest further.

The form of the equation (1.2.1) shows that the displacement vector \mathbf{u} is the eigenvector of the tensor Γ_{il} corresponding to the eigenvalue ρv^2 . Thus, the phase velocities and the polarizations of plane waves propagating in the direction \mathbf{n} in a crystal with stiffness tensor c_{ijkl} are given by the eigenvalues and eigenvectors of the tensor

ⁱ Here and further, the vectors are formatted bold. We will also identify the displacement vector with the polarization vector because actual amplitude of the sound wave plays no role in the current analysis.

Γ_{il} . As usual, the symmetrical three-dimensional stiffness tensor of fourth rank is reduced to a 6×6 matrix notation with indices ξ, ζ ranging from 1 to 6, such that

$$c_{\xi\zeta} = c_{ijkl}, \quad (1.2.3)$$

and pairs of the tensor indices $(ij), (kl)$ are renumbered as follows:

$$(11) \leftrightarrow 1, \quad (22) \leftrightarrow 2, \quad (33) \leftrightarrow 3, \quad (23) = (32) \leftrightarrow 4, \quad (13) = (31) \leftrightarrow 5, \quad (12) = (21) \leftrightarrow 6. \quad (1.2.4)$$

For a given direction, there are three phase velocities which are the solutions of the secular equation

$$\left| \Gamma_{il} - \rho v^2 \delta_{il} \right| = 0, \quad (1.2.5)$$

where δ_{il} is the Kronecker delta. For each velocity there is a corresponding eigenvector giving the direction of the displacement of the material, i.e. the wave polarization. Thus, in general, three plane waves with different velocities and with orthogonal polarizations can propagate in the same direction,. The displacement vector \mathbf{u} is not generally parallel or perpendicular to the wave normal \mathbf{n} . The wave with polarization closest to \mathbf{n} is called quasi-longitudinal (QL), and the others are called quasi-transverse, or quasi-shear waves (QS).

In the anisotropic medium, the direction of the ray velocity vector \mathbf{V}_e (also called the group velocity vector) determines the propagation direction of energy and does not coincide, in general, with the direction of the wave normal \mathbf{n} . Vectors \mathbf{V}_e and \mathbf{n} are related by expression

$$\mathbf{V}_e \cdot \mathbf{n} = v, \quad (1.2.6)$$

that shows the projection of the ray velocity onto the wave normal is equal to the phase velocity. Thus, the knowledge of the stiffness tensor $c_{\xi\zeta}$ of an anisotropic material (a crystal) allows one to find all the parameters of the propagating *plane wave* if the direction of its wave vector \mathbf{K} , which coincides with the direction of the wave normal \mathbf{n} , is known.

Reflection and refraction of plane harmonic waves at the plane interface between two different anisotropic media (crystals) can be efficiently analyzed by the method using the slowness surfaces (curves) and the slowness vector. The latter, which sometimes called the refraction vector [3], is introduced as vector

$$\mathbf{m} = \mathbf{n}/v = \mathbf{K}/\omega, \quad (1.2.7)$$

where $\omega = 2\pi f$ and f is a frequency of the elastic wave. The locus of the vector \mathbf{m} in the space of inverse velocities ("slownesses") forms a slowness surface, which are of use when finding directions of reflected and refracted waves. The procedure developed for that [**Error! Bookmark not defined.**, **Error! Bookmark not defined.**] is based on the fact that projections onto the interface of the slowness vectors of all those waves have to be equal to the projection of the slowness vector of the incident wave. In this report, this procedure will further be applied to find conditions of total internal reflection of the slow shear wave in TeO_2 while designing the TIRUS body.

Amplitudes of each of the reflected and refracted waves can be found from the equations [2, p. 235]

$$u_i^I + \sum_R u_i^R = \sum_T u_i^T, \quad (1.2.8)$$

$$c_{ijkl} l_j \left(K_l^I u_k^I + \sum_R K_l^R u_k^R \right) = c'_{ijkl} l_j \sum_T K_l^T u_k^T \quad (1.2.9)$$

derived from the continuity condition for stresses and displacements on the interface. Here c'_{ijkl} are the stiffness constants of the second medium, l is the unit vector normal to the interface; upper indices I , R , and T are related to the incident, reflected and transmitted (refracted) waves respectively. If the second medium is absent (that is, the interface is a free surface of the crystal), equation (1.2.9) becomes

$$c_{ijkl} l_j \left(K_l^I u_k^I + \sum_R K_l^R u_k^R \right) = 0. \quad (1.2.10)$$

One consequence from this equation, namely the fact that *at any angle of incidence an incident shear wave polarized parallel to a free reflecting surface of the crystal is totally reflected* [2, p.237], that is, *does not generate any wave modes except ones with the same polarization*, will be of great importance in our further analysis (see sections 4.2 and 5.1.1).

The procedure for finding reflected and refracted waves applied to some cases of the plane wave reflection in TeO_2 is illustrated in Figs. 1.2.2 and 1.2.3 (see the next page). The incident slow shear wave propagates in the crystallographic direction $[110]$ and is polarized along $[\bar{1}\bar{1}0]$, that is perpendicularly to the plane of the drawing. The plane of incidence and the crystallographic plane $(\bar{1}\bar{1}0)$ coincide with it. The interface, represented by a thick black line, separates the TeO_2 crystal and the medium of the Object Under Test. The projection of the slowness vector \mathbf{m}^I of the incident wave onto the interface is found using the green auxiliary vector: the intersection of the green line starting from its end and normal to the interface with the slowness surface gives a point towards which the slowness vector \mathbf{m}^R of the reflected wave is directed.

A conventional procedure for finding the slowness surface for any of three orthogonally polarized waves propagating in an arbitrary direction can be described as follows: (1) three eigenvalues ρv_i^2 , $i=1, 2, 3$, and three eigenvectors \mathbf{u}_i of the Christoffel tensor Γ_{il} are found for a given direction of the wave normal $\mathbf{n}(\theta, \varphi)$; (2) a function $v_u(\theta, \varphi)$ is calculated, where v_u is the velocity of the wave of a selected polarization \mathbf{u} ; (3) a magnitude of its slowness vector $|\mathbf{m}_u(\theta, \varphi)|$ depending on direction of the wave normal $\mathbf{n}(\theta, \varphi)$ is found. The spherical polar angles θ and φ of the wave normal are defined in Fig. 1.2.1.

Analysis of behavior of the three waves propagating in plane $(\bar{1}\bar{1}0)$ of TeO_2 ($\varphi = \text{const} = 45^\circ$) shows that one of them, slow shear wave, is polarized along $[\bar{1}\bar{1}0]$ and its polarization does not depend on θ . The phase velocity of this wave can be found analytically [5]

$$v(\theta) = \sqrt{\frac{1}{\rho} \left[c_{44} + \left(\frac{c_{11} - c_{12}}{2} - c_{44} \right) \sin^2 \theta \right]}. \quad (1.2.11)$$

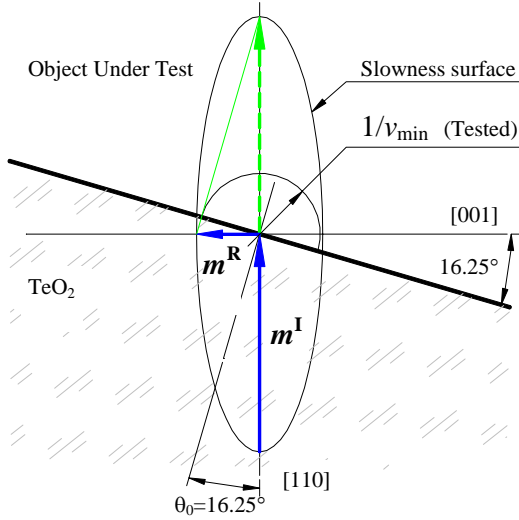


Fig. 1.2.2. Reflection of the plane slow shear wave in plane (110) of TeO₂: the "purest case" – the incident and reflected waves propagate along the axes of symmetry. Directions of the phase and the ray velocities coincide.

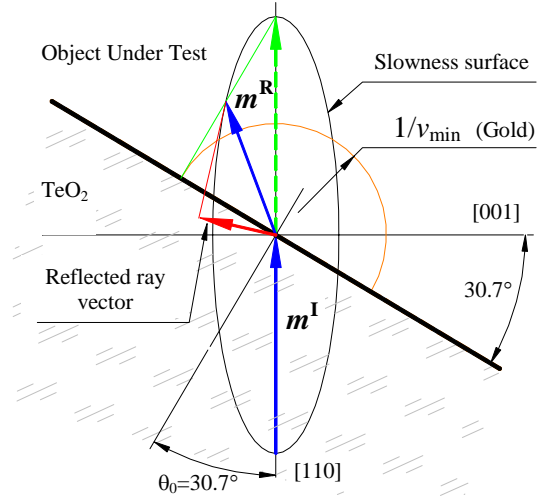


Fig. 1.2.3. Reflection of the plane slow shear wave in plane (110) of TeO₂: an "odd case" – the slowness (or wave) vector of the reflected wave and its ray vector shows toward different sides of the interface between the TeO₂ crystal and an object under test.

Thus, for cases presented in Figures 1.2.2 and 1.2.3, the common procedure is reduced to calculation of the slowness vector magnitude $|m(\theta)| = 1/v(\theta)$ found from equation (1.2.11).

In all calculations, the following values of material constants of TeO₂ have been used [6]: $c_{11}=5.57$, $c_{12}=5.12$, $c_{13}=2.18$, $c_{33}=10.58$, $c_{44}=2.65$, $c_{66}=6.59 \times 10^{10}$ N/m²; $\rho=5.99 \cdot 10^3$ kg/m³.

Two cases corresponding to two different angles of incidence θ_0 , 16.25° and 30.66°, have been analyzed. The angle of incidence equal to $\theta_0=16.25^\circ$ was calculated using expression [7]

$$\theta_0 = \arctan \sqrt{(c_{11} - c_{12}) / 2c_{44}} . \quad (1.2.12)$$

In this case, which, in a sense, is the "purest" one, the reflected wave propagates along the four-fold axis of symmetry [001] of the TeO₂ crystal, which coincides with axis X_3 of the Descartes coordinate system (see Fig 1.2.1). Its phase and group (ray) velocities coincide as well. The part of a circle in the "Object Under Test" area is tangent to the normal (green line) to the interface. Its radius determines a minimum sound velocity $v_{\text{ext}}=v_{\min}$ in an external isotropic medium for which a total internal reflection is still observed. Indeed, for faster waves with greater velocities their slowness surfaces lie within the circle and no intersections with the green line are possible. For the case considered, a simple geometrical calculation gives the minimum velocity equal to $v_{\min}=v^I/\sin\theta_0=613/0.279=2190$ m/s, where v^I is the phase velocity of the incident slow shear wave. Thus, the total internal reflection will only be observed for materials in which the shear wave velocity is greater than 2190 m/s. No waves except those having the same polarization as the incident one will be generated at its reflection because its displacement vector lies exactly in the interface plane. Therefore, only such waves are taken into account. (According to "seismological terminology" it has a shear-horizontal polarization being a SH-wave).

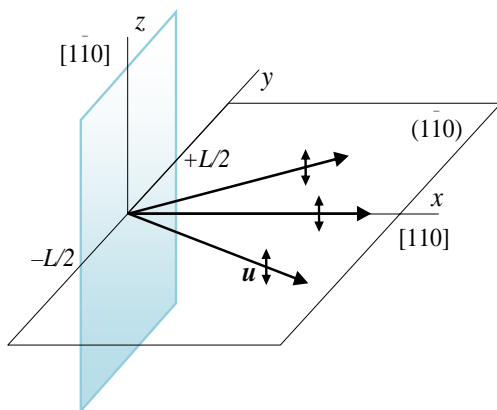
The second case is presented in Fig. 1.2.3. The angle of incidence is increased up to 30.66° and the minimum velocity v_{\min} becomes $v_{\min\text{Au}}=1200$ m/s equal to the velocity of the shear wave in gold. This material is

chosen for illustration as a metal with the smallest (except bismuth) sound velocity [8]. Geometrical constructions here are the same as in Fig. 1.2.2 but the results are drastically different: the ray vector (red) and the slowness vector \mathbf{m}^R (blue) of the reflected wave are directed to opposite sides of the interface. Nevertheless, the reflected wave exists and its energy propagates along the ray vector inwards the TeO_2 crystal. The total internal reflection of the incident wave will be observed for all materials in which the shear wave velocity is greater than 1200 m/s.

From the conducted analysis, one can infer that there could be a lot of designs of the TIRUS body depending on a specific application. It is important to emphasize however, that the described procedure and geometrical constructions considered in this section are only applicable to the plane waves. More complicated cases we analyze in the next one.

1.2.2 The Fresnel zone of the emitting transducer and ultrasound beams in TeO_2

The conventional technique used to study reflection of the plane waves can be applied to the wave beams, that is, to the spatially limited wave fields. Methods based on the Fourier decomposition of the wave field into an angular spectrum of plane waves are well known and can be helpful for calculation of the field of the reflected beam in isotropic media (see [9, §14], for example). An alternative approach involving Green's dyadic displacement tensor function [10] can probably also be of use. As to our knowledge, however, for the time being there is no similar comprehensive technique, which could be applied to the crystal of an arbitrary symmetry or even to the tetragonal one to which TeO_2 is related. In our case, additionally, the question arises of which criteria should be used to determine the beam boundaries in the TeO_2 crystal of a limited size because its reflecting plane can be lie well within the near field, or the Fresnel zone, of the emitting transducer.



1.2.4. Polarization of the slow shear waves propagating in plane $(1\bar{1}0)$ of TeO_2 .

Distribution of the sound intensity in the near field of the slow shear wave in plane $(1\bar{1}0)$ of TeO_2 can be calculated using an approach developed by Cohen [4]. He calculated fields of longitudinal elastic waves in crystals of cubic (Silicon) and trigonal (Quartz) symmetry and introduced an anisotropy parameter b , very beneficial while calculating a wave field in the vicinity of specific crystallographic directions. Since he considered longitudinal waves whose polarization did not depend on their directions, he had been able to transfer results obtained in optics to ultrasound. His results can be directly used in our case

because, as calculations show, polarization of the SSW propagating in the $(1\bar{1}0)$ plane does not change with its direction. This fact is illustrated in Fig. 1.2.4: all the displacement vectors are perpendicular to plane $(1\bar{1}0)$ independently of the wave direction. The coordinate system (x, y, z) introduced in Fig. 1.2.4 is tied to the transducer and has nothing to do with crystallographic axes of the crystal. Following [4] and using the slowness surface

calculated in the previous section, for the SSW propagating near direction [110] in TeO₂ one can calculate the anisotropy parameter

$$b_{110} = \frac{1}{2} \left(1 - \frac{m_{001}^2}{m_{110}^2} \right) = \frac{c_{11} - c_{12} - 2c_{44}}{2(c_{11} - c_{12})} = -5.4, \quad (1.2.13)$$

where m_{001} and m_{110} are magnitudes of the slowness vectors along directions [001] and [110] respectively. Once this parameter is known, the ultrasonic intensity distribution $I(x,y)$ can easily be calculated [4]:

$$I(x, y) = |S_0|^2 \sqrt{2}^{-1} \left| \int_{\mu^-}^{\mu^+} dv \exp\left(-\frac{1}{2}i\pi\mu^2\right) \right|^2, \quad (1.2.14)$$

where

$$\mu = \sqrt{2/\Lambda_0 x(1-2b)}(y_0 - y) \quad \text{and} \quad \mu \pm = \sqrt{2/\Lambda_0 x(1-2b)}(\pm L/2 - y). \quad (1.2.15)$$

Here S_0 is complex amplitude of the ultrasonic wave on the surface of the emitting transducer, Λ_0 – its wavelength along the axis, L – the size of the emitting transducer; y_0 stands for the y -coordinate in the plane of the transducer. Assuming $S_0 = \text{const} = 1$, substituting (1.2.14) into (1.2.13) and integrating over $\mu \pm$ interval we get the expression suitable for calculations:

$$u(x, y) = (1-i)\sqrt{\pi} \left[\text{erf}\left(-\frac{(1+i)\sqrt{\pi}(L-2y)}{2\sqrt{2(1-2b)x}\Lambda_0}\right) - \text{erf}\left(\frac{(1+i)\sqrt{\pi}(L+2y)}{2\sqrt{2(1-2b)x}\Lambda_0}\right) \right] / 2\sqrt{2}. \quad (1.2.16)$$

Here $u(x,y)$ – the ultrasonic amplitude distribution, erf – the error function. The intensity I distribution is calculated simply as $I(x,y) = |u(x,y)|^2$.

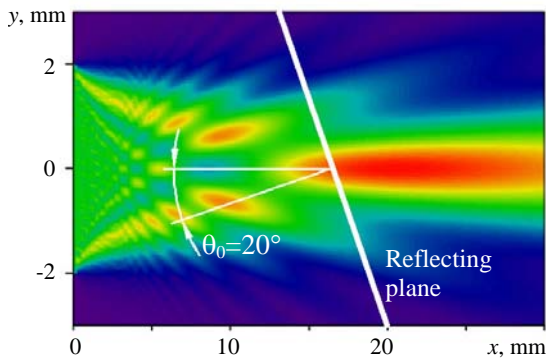


Fig. 1.2.5. The intensity field of an ultrasonic transducer emitting into the [110] direction of TeO₂. The drawing plane coincides with the crystallographic plane $(\bar{1}\bar{1}0)$. The rendered coordinates (x, y) are connected with the transducer and has nothing to do with crystallographic axes of TeO₂. The transducer size $L=4$ mm, the ultrasonic frequency $f=27$ MHz.

of the order of 15-20° it will be located just at the "starting point" of the beam. At the same time, since the reflecting plane is necessarily oblique, a distribution of the incident beam field on it can be rather heterogeneous.

The results of calculations carried out for the transducer size $L=4$ mm and sound frequency $f=27$ MHz are presented in Fig. 1.2.5. These values for the transducer size and the frequency were taken as practical ones suitable for the TIRUS body design. As shown in [4], the calculated intensity distribution at a distance x from the transducer is equivalent to that in the isotropic case at a distance $x(1-2b)$. For TeO₂, $b=b_{110}=-5.4$ is negative, so the Fresnel zone of the transducer becomes shorter by 11.8 times and ranges up to ~20 mm, at a distance, where a smooth ultrasonic beam starts shaping. This distance is one at which it is reasonable to place a reflecting plane of the TIRUS, as it is shown in Fig. 1.2.5. For angles of incidence θ_0 of

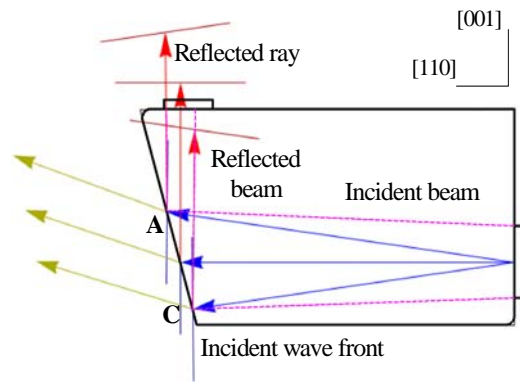


Fig. 1.2.6. Illustration of the heuristic procedure developed to determine boundaries of ultrasonic beams. Axes in the upper right corner show orientation of the sensor body relative to crystallographic directions. Blue and red arrows represent rays of incident and reflected divergent beams. Boundaries of the beams are shown with magenta dash lines. Yellow arrows on the left represent hypothetical refracted rays transmitted into gold. Geometrical constructions are based on calculation of sound field distribution represented in Fig. 1.2.5 and carried out according to the illustrated procedure.

The task of finding a reflected field of a heterogeneous incident beam was not being solved in the frame of the current project. Nevertheless, the need in a guide to trace incident and reflected beams was evident for finding the sensor body geometry. In the course of the project execution, the following heuristic procedure illustrated in Fig. 1.2.6 was applied to determine boundaries of the beams:

1. The incident beam was assumed to be of a simple structure consisting of rays divergent from the transducer (blue vectors in Fig. 1.2.6).
2. Two points, A and C, corresponding to a predetermined level of the sound intensity on the reflecting plane were chosen.
3. Boundaries of the incident beam were determined as lines (dash magenta) connecting the chosen points with the transducer edges. These lines were

not equal to the mentioned rays; they were simply assumed to be "geometrical boundaries" of the radiated beam.

4. The blue vectors striking the chosen points were assumed to be the *boundary rays* of the incident beam.
5. Directions of the *boundary slowness vectors* of the incident beam were found *given that its boundary rays had been found* at the previous step.
6. Directions of the *boundary slowness vectors of a reflected/refracted beam* were found using the conventional procedure for plane waves described in Section 1.2.1 given that the *incident boundary slowness vectors* had been found at the previous step.
7. *Boundary rays of the reflected beam* (red vectors) were found *given that its boundary slowness vectors* had been found at the previous step.
8. Intersection of the reflected boundary rays with the upper crystal surface carrying a receiving transducer provided two of four boundary points of the reflected beam. Other two were ones on the reflecting plane marked as A and C. Connecting lines (dash magenta) were "geometrical boundaries" of the reflected beam.

The described procedure was put into the base of the software developed to simulate propagation and reflection of the SSW ultrasonic beams in the $(1\bar{1}0)$ plane of TeO_2 while designing the sensor body. It simulated not only the ray directions of the plane waves composing ultrasonic beams but their wave fronts as well: those are shown in Fig. 1.2.6 as poked lines at the ends of the ray vectors.

1.2.3 Simulation of ultrasonic beams propagation and reflections

Simulation of behavior of ultrasonic beams propagating and reflecting from surfaces of a limited size TeO_2 crystal becomes necessary when a design of an experimental sample of the TIRUS body is developed. The software developed in the frame of the current project allowed a designer to track such behavior while changing geometry of the sensor body and positions of both emitting and receiving transducers.

The calculation algorithm of the heuristic procedure described in the previous section was realized as follows. A reflecting plane in Fig. 1.2.5 was represented by the line determined by equation $x=ky+C$, and distribution of the ultrasonic intensity $I(x,y)$ across it was calculated from equation (1.2.16). Then, the y values y_{b1} and y_{b2} were found corresponding to the ultrasonic intensity level

$$I_{level} = I_{max} \cdot 10^{-A_{dB}/10}, \quad (1.2.17)$$

where I_{max} is a maximum value of the intensity across the line and A_{dB} is its predetermined value in dB related to I_{max} .

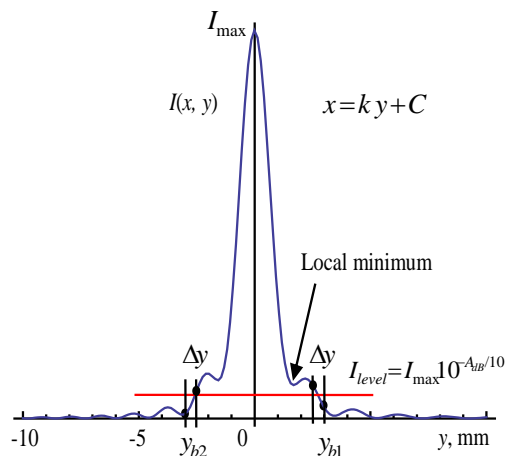


Fig. 1.2.7. Distribution of the sound intensity across the reflecting plane. The drawing plane coincides with plane $(\bar{1}\bar{1}0)$ of TeO_2 . The coordinates (x, y) are connected with the transducer and but not with crystallographic axes of TeO_2 . The transducer size $L=4$ mm, the ultrasonic frequency $f=27$ MHz.

The whole calculation procedure is illustrated in Fig. 1.2.7 where distribution of the sound intensity on the reflecting line is presented. The coordinate system is tied to the transducer (as in Fig. 1.2.4). The beam boundaries are found by means of moving step by step along y outwards the transducer axis ($y=0$) until the intensity value I_{level} is achieved. The found values y_{b1} and y_{b2} determine the beam boundaries at the given line, that is, at points A and C in Fig. 1.2.6. These values were found with precision up to the step interval Δy that in calculations had been chosen 0.03 mm. This crude procedure has been used instead of a conventional numerical method, such as Newton's one for example, as long as it worked better because of unevenness of the $I(x,y)$ function.

An interface software providing interaction between an operator and the calculation procedure has been developed to operate in a Windows environment. It allows to choose any configuration and size of the crystal as well as a size and a position of the emitting transducer. It maps geometry of the incident, reflected and refracted ultrasonic beams dependent on the chosen sensor body geometry and given parameters: the ultrasonic frequency f , predetermined level of the ultrasonic intensity A_{dB} and the sound velocity v_{ext} in an external medium contacting with the reflecting surface of the TeO_2 crystal. Direction of the boundary and central vectors of the beams are also can be displayed.

An example of the results obtained with the developed software is presented in Fig. 1.2.8 (see the next page). A gray table in the lower part of the figure displays global parameters put into the program as initial ones. The table on the left hand side displays calculated directions of the wave vectors and the rays (the group velocities) tied to the three chosen points on the reflecting plane, the central one "B" and the boundary ones "A" and "C". From the data displayed, one can see that for the incident rays "A" and "B" the total internal reflection is observed because corresponding refracted rays are directed along the interface. On the contrary, the incident boundary ray "C" is refracted and propagates in the external medium.

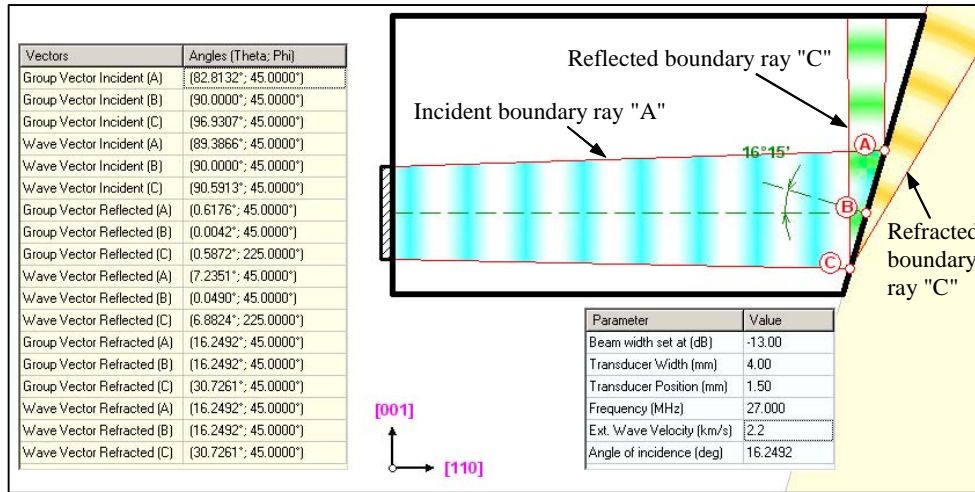


Fig. 1.2.8. Simulation of propagation and reflection of the slow shear wave beam in plane $(\bar{1}\bar{1}0)$ of TeO_2 . The intensity of the sound field at points A and C on the reflecting plane is chosen -13 dB related to the maximum one, the ultrasonic frequency is 27 MHz, the transducer size 4 mm.

2 Sensor design and fabrication

2.1 Choice of the sensor geometry

An experimental sample of the TIRUS has been designed using the simulation software described in the previous section. The ultimate geometry of the sensor body had to meet a number of requirements. Firstly, the crystal size had to be large enough for the reflecting plane to be placed out of the Fresnel zone of the emitting transducer. Secondly, an ultimate design had to be chosen in such a way to provide total internal reflection of an incident ultrasonic beam from the interface for a wide variety of tested materials. Additionally, it had to be compatible with the technology of the vacuum diffusion welding that was used for fabrication of the experimental samples. The last, but not the least, was that it had to enable the technology of the optical contact for assembly of the sensor and an object under test to experiment with.

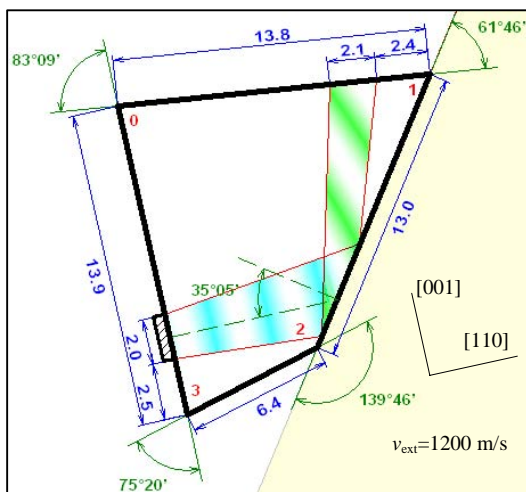


Fig. 2.1.1. The sensor body geometry providing the total internal reflection of the incident ultrasonic beam for a wide variety of tested materials.

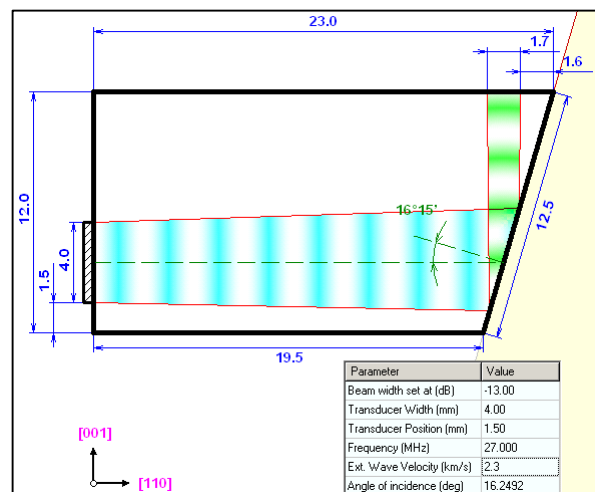


Fig. 2.1.2. The sensor body geometry accepted as suitable for fabrication of an experimental sample of the TIRUS. The sizes are given in mm.

An outline of the sensor body geometry suitable to operate with a wide variety of materials is presented in Fig. 2.1.1. When it was designed, one of the global parameters, the sound velocity in an external material v_{ext} was chosen to be 1200 m/s. Thus, for all materials with greater shear wave velocities the total internal reflection was provided. It was achieved due to a large value of the angle of incident equal to 35° . This quirky geometry looks very attractive as to be applicable to many tested materials but it obviously does not meet other requirements listed above. Therefore, a design realizing "the purest case" has been taken as suitable for an experimental sample. It is presented in Fig. 2.1.2. The faces of the crystal carrying both the emitting and the receiving transducers are normal to $[110]$ and $[001]$ crystallographic directions respectively. The emitting transducer size of 4 mm provides rather narrow ultrasonic beam not touching the side faces of the crystal. The minimum length of the body along the $[110]$ direction is 19.5 mm providing thus the place for the reflecting place across a smooth part of the sound beam, as it is shown in Fig. 1.2.5. The design also provides total internal reflections for all the plane wave components of the ultrasonic beam if the external wave velocities are equal to 2300 m/s or more.

2.2 Sensor fabrication

An initial "blank crystal" used to fabricate a sensor body was a rectangular specimen of single-crystal TeO_2 . The size of the crystal was $23[110] \times 12[001] \times 10[110]$ mm. With respect to the crystallographic coordinates, its faces were oriented with accuracy not worse than $\pm 2'$. As long as further optical investigations were supposed, all faces of the initial specimen were polished with all necessary precautions to save their orientation.

Two piezoelectric plates of a few millimeter thicknesses were bonded to the corresponding surfaces of the crystal using technology of vacuum diffusion welding and then ground to a necessary thickness. After that, a reflecting face was made. A sensor body with ready transducers and an inclined reflecting face is presented in Fig. 2.2.1. The piezoelectric plate of the receiving transducer on the upper face of the crystal has two separated electrodes. It has been done to have an option to select a different position of the "virtual" receiving transducers

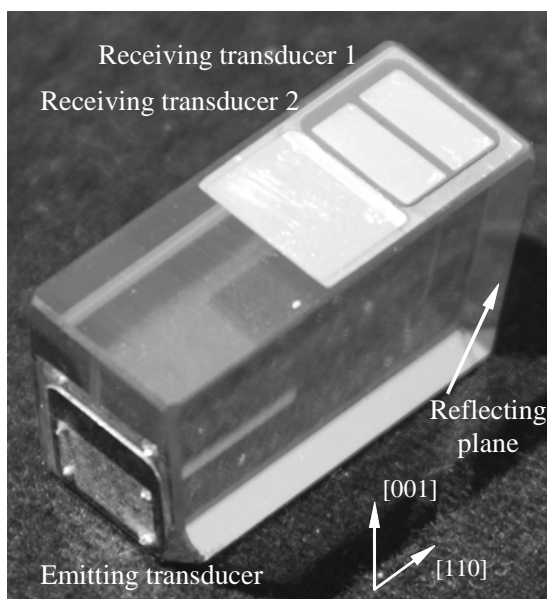


Fig. 2.2.1. The sensor body with bonded piezoelectric transducers. The reflecting plane is inclined by $16^\circ 15'$.

1 and 2 in further experiments with the sensor as a two-port network. The reason for that was possible inaccuracy in a proper calculated position of the receiving transducer, which could be caused by heuristic procedure developed to define boundaries of the ultrasonic beams.

An important step in fabrication of the sensor body is verification of its (110) face orientation, that is, the plane to which the emitting transducer is bonded. It is connected with the fact that insignificant inclination in the plane (001) of the wave normal, that is, the emitting transducer axis from crystallographic direction $[110]$ causes significant obliquity of the emitted sound beam [11]: for example, if it deviates by $30'$, the sound beam

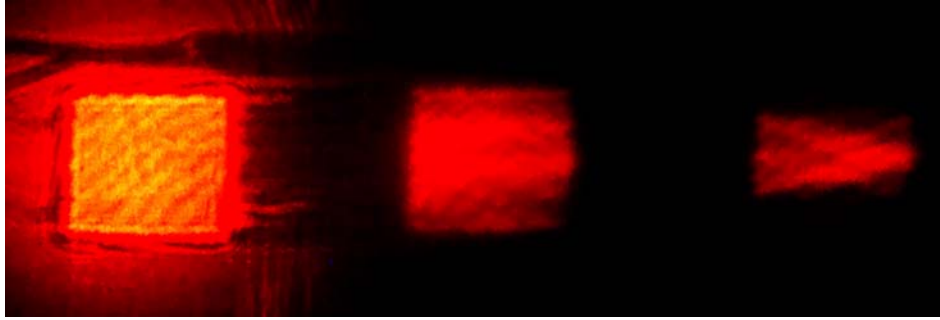


Fig. 2.2.2. The light diffraction pattern representing the sound field distribution in the (001) plane. Two diffraction orders are observable. Overexposed image on the left represents non-diffracted light beam. The transducer is on the left side of the crystal. The input signal frequency is 27 MHz, pulse modulated. Pulse duration is 3 μ s, repetition rate 30 kHz.

deviates by $\sim 25^\circ$.

Verification has been carried out by means of optical visualization of the sound beam using an acousto-optic technique. A beam of a He-Ne laser was extended up to a few centimeter to illuminate the (001) face of the crystal (the upper one in Fig. 2.2.1). The emitting transducer generated a 27 MHz ultrasonic wave modulated by pulses of 3 μ s duration with repetition rate of 30 kHz to avoid resonances of the TeO₂ crystal. The expanded light beam was affected by the ultrasonic wave and a light diffraction pattern shown in Fig. 2.2.2 was observed.

An over-exposed image of the part of the crystal itself free of the metallic electrode is observed at the left hand side of the figure. The first diffraction order is observed in the middle, and at the right hand side – the second one. Efficiencies and angular positions of these two orders differ significantly, therefore each single one of them one displays different details of the sound beam structure. For the time being though, the only one feature of the visualized sound beam is important for us – its inclination from the [110] direction that is practically undetectable. From which one can conclude that the crystal faces are oriented precisely enough and the "blank crystal" used to fabricate an experimental sample of the TIRUS proved to be suitable for this purpose.

Piezoelectric transducers bonded to the TeO₂ crystal were fabricated from the 163° Y-cut plates of lithium niobate. From their original thickness of ~ 2 mm they were ground and polished down to a thickness of 82 μ m for the emitting transducer and to 78 μ m for the receiving one. That was done to provide the same resonance frequency of 27 MHz for transducers loaded on considerably different acoustic impedance caused by a significant difference between the sound wave velocities along the [110] and [001] directions of TeO₂, 613 m/s and ~ 2103 m/s respectively. A procedure applied to necessary correction of the transducer thickness is described in [12]. The size of the emitting transducer was 4[001] \times 6.5[110] mm, sizes of both receiving ones were 2.5[110] \times 6.5[110] mm.

Input impedance of both fabricated transducers was measured using Network Analyzer HP3577A. While doing measurements, acoustic resonances of the sensor body were smoothed by means of filtration to avoid their influence on measured characteristics. Obtained results showed that thickness of the emitting transducer was chosen correctly (its resonance was close to 27 MHz), and resonance of the receiving one was shifted up to almost 30 MHz. Nevertheless, it caused no difficulties in further matching of the transducer. Matching circuits

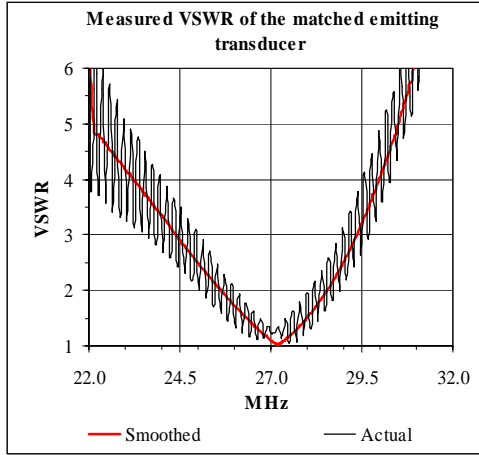


Fig. 2.2.3. VSWR of the sensor input vs frequency.

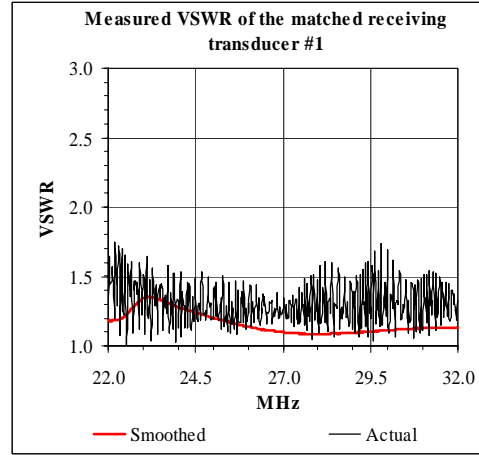


Fig. 2.2.4. VSWR of the sensor output vs frequency.

were simple L-C sections for both transducers. The measured voltage standing wave ratios (VSWR) of the ultimate construction of the TIRUS are presented in Fig. 2.2.3 and 2.2.4. Characteristics named "Actual" were measured without any filtration, and therefore represent acoustic resonances of the TeO_2 crystal. One can see VSWR does not exceed 1.5 at 27 MHz that provides the reflection losses of the transducers less than 0.2 dB.

3 Experimental studies of the sensor as a two-port network

3.1 Study with a continuous wave signal

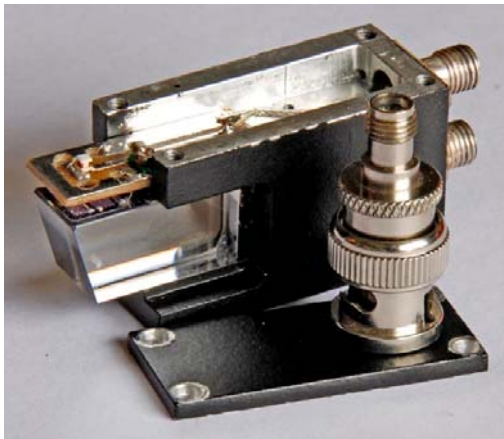


Fig. 3.1.1. Appearance of the ultimate TIRUS construction. The upper cover is removed. The left oblique face of the crystal is the working surface of the sensor. The sensor output, an upper connector on the right, is connected to the receiving transducer on the upper face of the crystal through a matching network. The sensor input, a lower one on the right, is connected to the emitting transducer through a similar one hidden in the bottom part of the housing. A BNC-SMA adapter is shown as a measure.

The main idea of the TIRUS is to detect a change in the magnitude and/or the phase of an ultrasonic wave reflected from an interface between the sensor and an Object Under Test (OUT) in case of frustrated total internal reflection caused by a subsurface flaw. In this case, the TIRUS is treated as a two-port network with its input and output to be the emitting transducer and the receiving one respectively. An ultimate version of the TIRUS construction used in the continuous wave (CW) experiments is presented in Fig. 3.1.1. This design was also used in all further experiments with tested objects, both flawless and defective.

A natural way to characterize the TIRUS as a two-port device that enables tracking change of the reflected wave characteristics is to measure its own complex transmission coefficient

$$T = U_{\text{out}}/U_{\text{in}} = |T| \exp(i\phi), \quad (3.1.1)$$

to use it as a reference, and then to track its change in case of frustrated total internal reflection. Here U_{out} and U_{in} are complex voltage of the continuous wave signals at the output and the input of the device; $|T|$ is a magnitude of the transmission coefficient, ϕ is a phase shift caused by the device, which is usually called the insertion phase, and the logarithmic value defined as

$$IL = -20\log_{10}|T| \quad (3.1.2)$$

is the insertion loss.

In experiments, transmission coefficient of the TIRUS was measured using Network Analyzer HP3577A

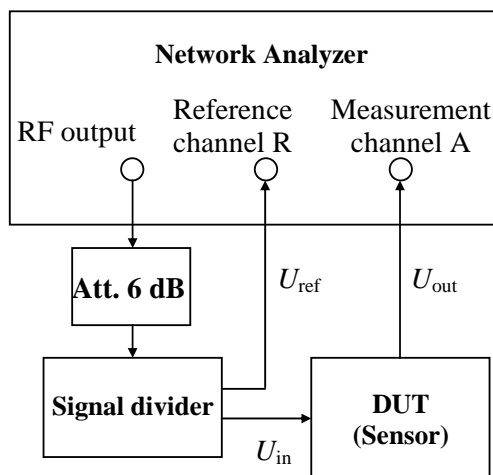


Fig. 3.1.2. A schematic of the measurement setup used in the continuous wave experiments.

with a technique schematically presented in Fig. 3.1.2.

A Device Under Test (DUT) was either the TIRUS itself when the reference data were acquired or an assembly TIRUS+OUT, where OUT could be any Object Under Test from those that were investigated in the course of the project. Theoretically, a signal in the reference channel U_{ref} could differ from a signal at the TIRUS input U_{in} , i.e., a measured transmission coefficient T could be not exactly that defined by equation (3.1.1). But, firstly, this difference could not be significant because input impedance of the TIRUS was close to 50 Ohm and, secondly, it did not matter because this coefficient once measured would be the same in all further experiments. The measurement procedure was carried out as follows:

1. The Network Analyzer input was chosen A/R, one of its displayed function was "Magnitude Log", another – "Phase". The DUT was removed and the measurement circuit was calibrated using operation "Normalize" in the frequency range of 50 kHz around 27 MHz.
2. The DUT was placed into the measurement channel and its transmission coefficient T (magnitude and phase) was measured. It corresponded to chosen input A/R of the Network Analyzer.
3. The "Normalize" operation could be repeated to remove the loss and phase shift inserted by the TIRUS itself. In this case, further measurements with an OUT would supposedly provide change of the transmission coefficient caused only by the tested object.

Results of measurements for two cases when one of the two receiving transducers #1 or #2 (see Fig. 2.2.1) was used as the TIRUS output are presented in Fig. 3.1.3 and 3.1.4 (see next page). They show that in case of the transducer placed in the calculated position (see Section 2.1) the insertion loss are much less than that for the shifted one. It means that the heuristic model used to simulate behavior of the ultrasonic beams in the limited TeO_2 crystal is good enough to predict a position of the reflected beam. At the same time, the measured value of the insertion loss turned out to be unexpectedly high; to see that, let us make some crude estimates of the expected ones.

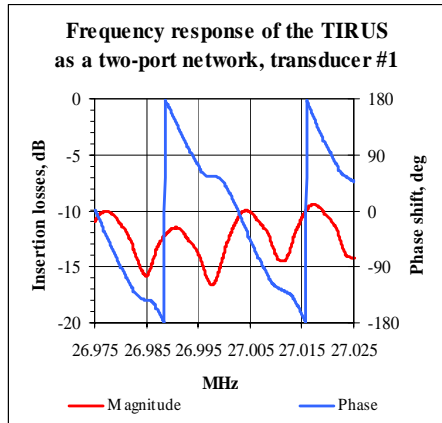


Fig. 3.1.3. The frequency response of the TIRUS with the receiving transducer located in a calculated position. The crystal is put into a preliminary housing distinguishing from the ultimate one presented in Fig. 3.1.3.

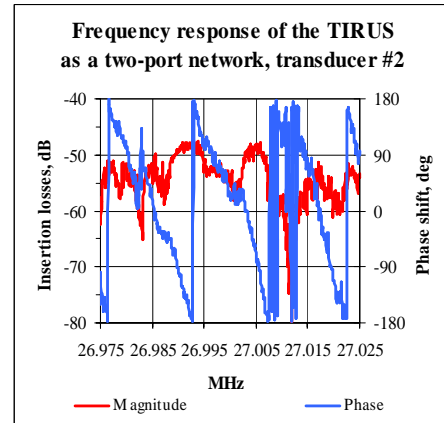


Fig. 3.1.4. The frequency response of the TIRUS with the shifted receiving transducer. The crystal is put into a preliminary housing distinguishing from the ultimate one presented in Fig. 3.1.3.

Main physical mechanisms causing insertion losses in the TIRUS, which essentially is a specific ultrasonic delay line, are:

- transduction loss TL including: (1) electrical reflection losses and dissipative losses in the matching networks; (2) dissipative losses in piezoelectric and bonding materials. At the measured $VSWR < 1.5$, the first one could be high. Let it be ~ 1.5 dB for two transducers together. Dissipative losses in the piezoelectric material, $LiNbO_3$, are negligible at 27 MHz (see, for example, [13]). Sound attenuation in the bonding material, Indium, is much greater than that in $LiNbO_3$, but given the fact that its thickness does not exceed $0.5 \mu m$ per the transducer, the estimated loss is hardly more than 0.5 dB for each one, if not negligible. Thus, total transduction losses can be estimated as $TL = 1.5 + 2 \times 0.5 = 2.5 < 3$ dB.
- propagation losses PL in the crystal, which include both attenuation losses (AL) and diffraction losses (DL). Attenuation of the slow shear wave along the [110] direction in TeO_2 is equal to 70 dB/cm at 500 MHz [14, p.184]. However, square dependence on frequency makes attenuation at 27 MHz be equal to $70 \times (27/500)^2 = 0.204$ dB/cm. Its path along [110] is ~ 2 cm (see Fig. 2.1.2) that results in the attenuation value ~ 0.4 dB. Thus, taking into account propagation of the sound wave along the [001] path as well, which is ~ 1 cm, let the total attenuation loss be $AL = 0.5$ dB. Estimation of diffraction losses is not such an easy task. Although studies dealing with the problem have been carried out since the fifties of the last century, results for shear waves in anisotropic medium seems to be hardly accessible. Therefore, let us simply "invent" some figures looking reasonable for our case. A conventional technique to estimate diffraction losses is to calculate the sound field radiated by the emitting transducer, to find the sound pressure distribution on the surface of the receiving transducer, to average it across its surface and get a result as a function of the distance between the transducers. Using this technique different researchers obtain very different results (see [15-§21, 16, 17] for example). As a rule, however, calculated diffraction losses DL do not exceed a few decibel, or even tenths of dB, if the distance D between the emitting and receiving transducers is less than a^2/Λ , where a is a characteristic size of the transducer, Λ is the sound wavelength. For an anisotropic medium [4]

$$a^2/\Lambda = (a^2/\Lambda)_{\text{isotr}}/(1-2b), \quad (3.1.3)$$

where b is the anisotropy parameter (see Section 1.2.2). In our case $v_{110}=613$ m/s, $f=27$ MHz, $b_{110} = -5.4$ that makes $a^2/\Lambda \approx 6$ cm. Taking into account the sensor body size (Fig. 2.1.2), we get $D < a^2/\Lambda$. Thus it looks reasonable, at least as an upper estimate, to let diffraction losses be "a few decibel", e.g. $DL=3-4$ dB. For total propagation losses that results in $PL=AL+DL=4-5$ dB.

- losses because of reflection of the sound beam from the free surface of the crystal RL . Those can be connected with: (1) scattering of the reflected beam by the reflecting surface that should be negligible because the reflecting plane was polished; (2) mode conversion. The latter also should not take place because the emitted sound wave is polarized along the $[1\bar{1}0]$ direction (see Section 1.2.1). So, it is reasonable to expect $RL \rightarrow 0$.

Summing all listed kinds of losses, one can expect the total estimated insertion loss TEL to be $TEL=TL+PL+RL \approx 7-8$ dB – a figure that looks reasonable.

As can be seen, the difference between measured (see Fig. 3.1.3) and the upper estimated losses lies within the range of 3-8 dB that is too large to be accidental and therefore is inexplicable. *Optical investigations in the next sections show, however, that mode conversions do take place which can be a reason for the observed difference.*

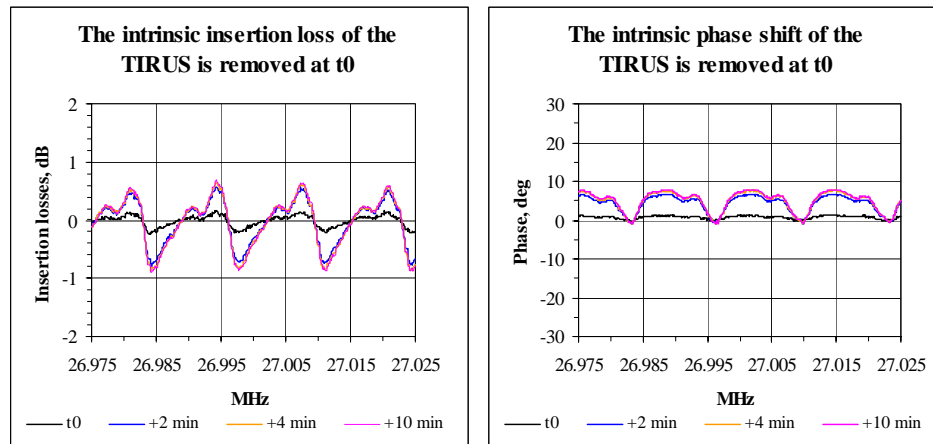


Fig. 3.1.5. Phenomenon of stationary points at the frequency response of the TIRUS. Both the insertion loss and the insertion phase change significantly vs time. At the same time, at some frequencies they stay stationary.

The frequency response of the TIRUS is of such a character that assumes acoustic resonances in the TeO_2 crystal. The measurements results which are presented in Fig. 3.1.5 reveal some unexpected features of the observed resonances. (In these measurements unlike those presented in Fig. 3.1.3 intrinsic loss of the TIRUS had been removed using the repeated "Normalize" operation). These figures demonstrate a significant instability of the transmission coefficient of the TIRUS: within a time interval of 10 min the insertion loss changes up to ± 1 dB and insertion phase up to 10° . In another experiment carried out some other day (its results are not put in the report) this change was up to ± 3 dB and 30° . In both cases however, some stationary points at the frequency scale were observed. Although we cannot suggest a comprehensive explanation of this phenomenon, it is obvi-

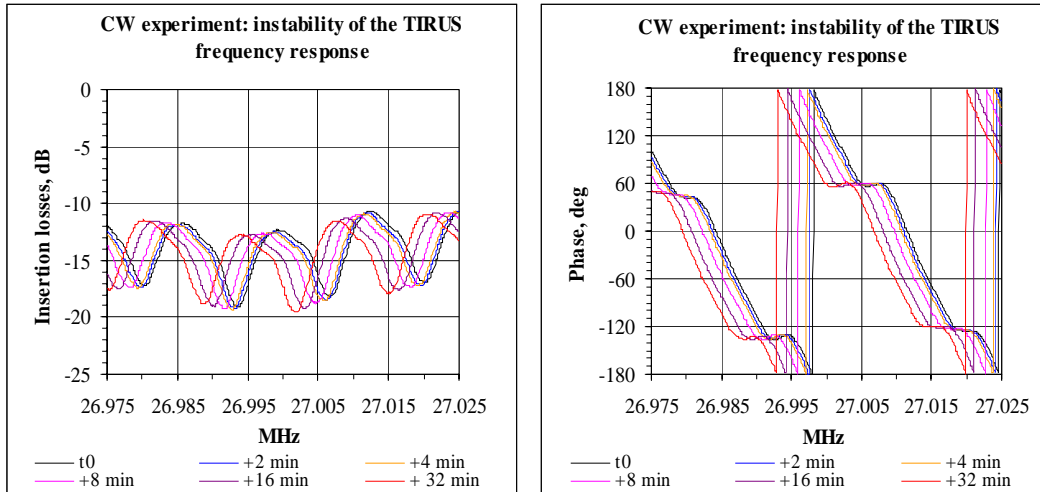


Fig. 3.1.6. Instability of the TIRUS frequency response.

ously connected with acoustic resonances because these points are placed through the same periodic intervals as characteristic points in Fig. 3.1.3.

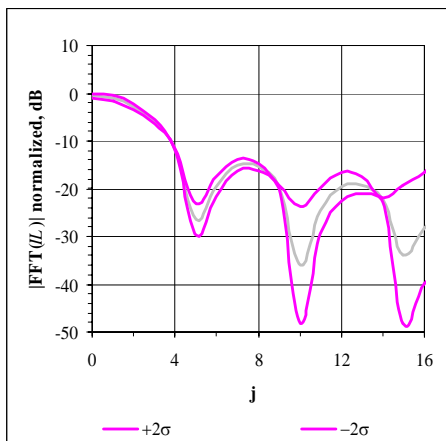


Fig. 3.1.7. Normalized FFT coefficients used in the continuous wave experiments as reference data. The $\pm 2\sigma$ curves show a 95% confidence interval. The gray curve represents the mean; σ is standard deviation.

The observed instability is a great obstacle to apply the technique using the TIRUS transmission coefficient as reference data for further experiments on detecting subsurface flaws in tested objects. Really, a change of the TIRUS frequency response even within one series of measurements (see Fig. 3.1.6) makes such "reference data" unreliable. On the other hand, the character of the change which is a kind of a simple shift along the frequency scale suggests a recipe for avoiding the obstacle. It could be a transformation invariant to shift. The most known such one is the Fourier transformation magnitude. Applying it to the TIRUS frequency responses one can expect to get reference data as a number of Fourier coefficients to which other transformed data could be compared. In this project, the Fast Fourier Transformation (FFT) was applied to a wide variety of measured characteristics

of the TIRUS to get reference data presented in 3.1.7. The $\pm 2\sigma$ value, where σ is standard deviation, defines a 95% confidence interval [18]. Once formed these reference data becomes an instrument for CW experiments with tested objects.

3.2 Study with time-gated signals

Another way to avoid acoustic resonances is to apply time-gated signals of duration significantly less than the propagation time of the ultrasonic wave in the sensor body, which is about $37 \mu\text{s}$. A schematic of the measurement setup used to realize this approach is presented in Fig. 3.2.1 (see the next page). A signal generator is modulated by rectangular pulses from a pulse generator, which also triggers an oscilloscope. The pulse duration

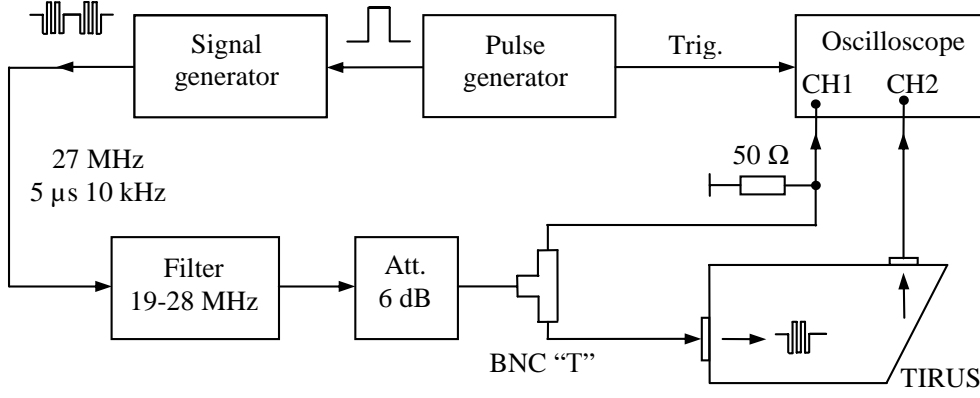


Fig. 3.2.1. A schematic of the measurement setup used in the experiments with time-gated signals.

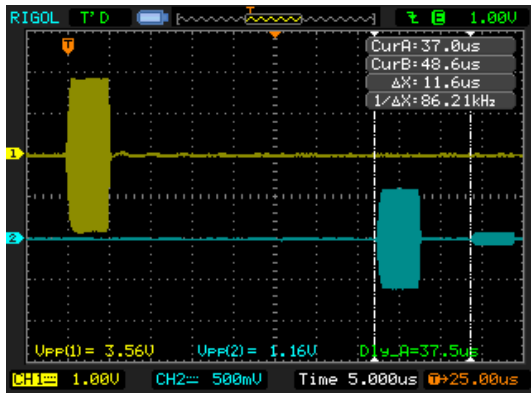


Fig. 3.2.2. A typical waveform acquired from the oscilloscope in the experiments with time-gated signals. The yellow RF pulse is a modulated sine wave at the TIRUS input, the blue ones – at its output. The sine wave frequency is 27 MHz, the pulse duration is 5 μs. Measured values are peak-to-peak voltage.

is controllable and in the experiments was 5 to 10 μs. The pulse repetition rate was 1 kHz. A typical waveform acquired from the oscilloscope is presented in Fig. 3.2.2. The peak-to-peak voltage was chosen as a measured value. In the presented case, which corresponds to a measurement of the TIRUS own parameters, the measured input peak-to-peak voltage $U_{pp_in}=3.56$ V (yellow number) and the output one $U_{pp_out}=1.16$ V (blue number). Their ratio yields the *real* "time-gated transmission coefficient"

$$T_{TG} = U_{pp_out} / U_{pp_in} , \quad (3.2.1)$$

which, unlike the transmission coefficient defined in the previous section, contains no phase information.

A two series of 10 measurements each of the TIRUS time-gated transmission coefficient provided its following reference value $T_{TG0}=0.327\pm0.027$ to which the results of experiments with flawless and defective objects were then compared. For example, for defective object #1 the measured value of T_{TG} was equal to 0.261 ± 0.011 that shows a significant effect caused by the defect. Other results are presented in Section "Results and discussion".

The 95% confidence interval $\pm 2\sigma$ shown for measured coefficients T_{TG} was as usually calculated from the known expression for dispersion σ^2 of indirect measurements [19, p. 13], which in our case of the ratio of two measured values U_{pp_out} and U_{pp_in} yields

$$\sigma = \sqrt{\left(\frac{\bar{x}_2^2 \sigma_1^2 + \bar{x}_1^2 \sigma_2^2}{\bar{x}_1^4} - 2\bar{x}_1 \rho_{12} \sigma_1 \sigma_2 / \bar{x}_1^3\right)} . \quad (3.2.2)$$

Here \bar{x}_1 and \bar{x}_2 are the means of measured values of the TIRUS input and output respectively, σ_1 and σ_2 are their calculated standard deviations; ρ_{12} is the correlation coefficient for input and output data, which certainly correlate because they were acquired within the same measurement operation.

4 Visualization of the sound beams in the sensor body

The heuristic approach developed in Section 1.2.2 to determine boundaries of the sound beam and to design the sensor body was based on a plane wave model. In the frame of this model, there should be no losses of energy of slow shear wave reflecting from the working surface of the sensor. Consideration of basic physical mechanisms leading to increase of the TIRUS insertion loss made in Section 3.1 shows that the estimated total loss value is much less than that observed in experiments. Therefore, detailed investigation of sound fields in the sensor body is of great importance to clarify possible reasons for this phenomenon. Optical visualization of ultrasonic beams in the sensor body is aimed at finding such reasons.

4.1 Experimental setup and technique

An experimental technique exploited in this section is based on studies of the light diffraction patterns caused by the ultrasonic beams propagating and reflecting in the sensor body. If the plane of incidence of the slow shear wave is the $(\bar{1}10)$ plane of TeO_2 , which is just the case (see Fig. 4.1.1a), visualization of these beams is of great difficulty because the acousto-optic interaction is forbidden [20] and the efficient photo-elastic coefficient $p_{eff}=0$. Nevertheless, it is possible, if the TeO_2 crystal is slightly inclined with respect to the direction of the probing light beam [7].

The optical part of the experimental setup consisted of a green laser (of 532 nm wavelength), a telescope, a polarizer, an aperture of an adjustable size of 2.5 to 30 mm and a 3-axis stage, which provided accurate orientation of the sensor body ("crystal") with respect to the axes of the optical system (Fig. 4.1.1). The angles of deviation of the crystal from the horizontal θ_h and from the vertical θ_v could be measured with accuracy of $\pm 1'$ and $\pm 5'$ respectively. The appearance of the experimental setup is represented in Fig. 4.1.2 (see the next page). The emitting transducer of the TIRUS (in the figure, on the left side of the sensor body) driven by a 27 MHz

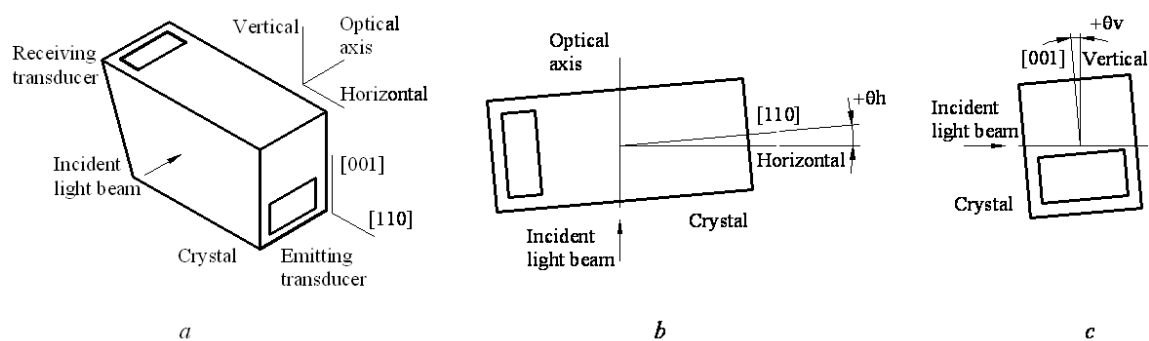


Fig. 4.1.1. *a* –The sensor body ("crystal") orientation with respect to the optical system axes, "Vertical", "Horizontal" and "Optical axis". *b* – the angle θ_h defines deviation of the crystal from the horizontal. *c* – the angle θ_v defines deviation of the crystal from the vertical.

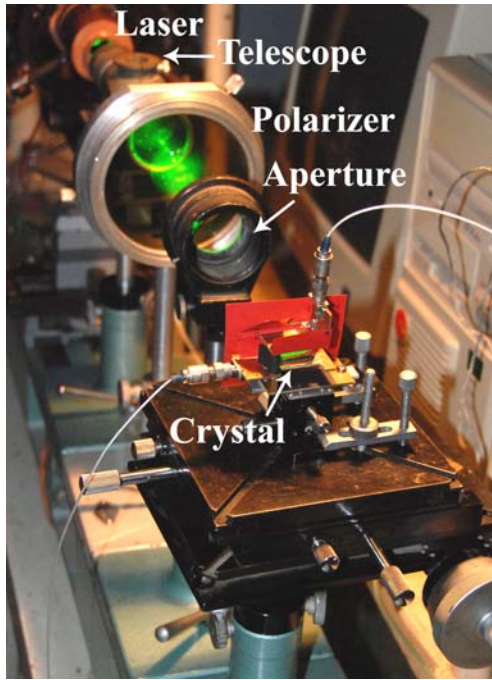


Fig. 4.1.2. Appearance of the optical part of the experimental setup.

continuous wave or a pulse modulated signal from a signal generator excited a slow shear wave that propagated along the [110] direction. An output signal from the receiving transducer was measured with an oscilloscope. The telescope was used to get a wide parallel light beam. The adjusted-size aperture was used to control the size of the light beam illuminating the crystal.

The light diffraction patterns were observed on a screen and photographed sequentially using two sizes of the aperture, large, ~30 mm and small, ~2.5 mm in diameter. The large-aperture experiment was conducted *to visualize ultrasonic beams*. A wide light beam was used to illuminate the entire crystal. In this case, despite the crystal is illuminated entirely, each specific "light response" is obtained only from the domain of the crystal where the sound beam exists. As a result, the whole beam can be visualized. If there are a lot of different sound beams propagating in the crystal, the responses

from all of them are overlaid and mixed, and the picture obtained is very complicated to analyze. On the contrary, when a small-size light beam is used, the diffraction spots are only derived from a specific area in the crystal illuminated by a narrow laser beam. An observed distinct Schaefer-Bergmann's pattern [21, Chap. 5] gives information about the type of the sound waves crossing the illuminated area.

4.2 Identification of the sound field structure

The main objective of visualization of the sound beams in the sensor body (crystal) carried out was to get data allowing us to understand why the measured insertion loss of the TIRUS treated as a two-port network was unexpectedly great. Another objective was to see to which extent the theoretical model put in the base of the sensor design was adequate to a real physical picture.

In the experiments, a pulse-modulated (PM) sine-wave was used to exclude interference of multiply reflected sound waves from the crystal boundaries. A continuous wave (CW) signal was used to reproduce the situation that took place when the insertion losses of the TIRUS were measured with the Network Analyzer. In both cases, the frequency of the signals was 27 MHz.

In the sequential experiments, a position of the camera was fixed what provided the same exact position of the exposed images on its photosensitive element enabling further combined processing of the obtained pictures. In each case, the three pictures were taken: one with the CW signal applied to the emitting transducer, one with the PM sine wave (pulse duration 10 μ s, repetition rate 10 kHz), and one with no signal at all. The presence of the no-signal picture enabled to extract a stray lighting from the initial picture. As a result, an ultimate processed image contained mainly only a response from the sound beams.

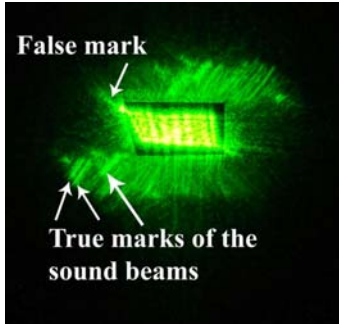


Fig. 4.2.1. A light diffraction pattern: the CW signal is applied.

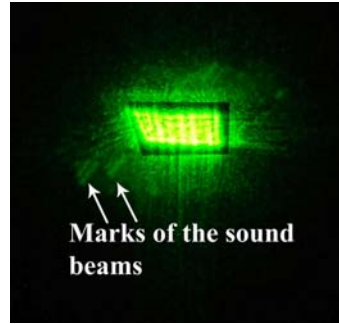


Fig. 4.2.2. A light diffraction pattern: the PM signal is applied.

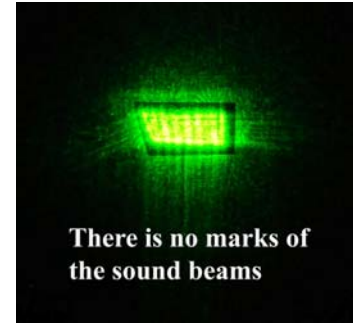


Fig. 4.2.3. A light diffraction pattern: no signal is applied.

Typical diffraction patterns are presented in Figs. 4.2.1-4.2.3. The first picture shows the pattern observed while a CW signal is applied. The central overexposed part of the picture is simply a spot of the wide laser beam passed through the crystal. Its brightness is suppressed by means of a non-reflecting zone (the black shadow within the illuminated area) on the white screen used for observations. "The hair" around the crystal image, which is represented by the black shadow, is the diffraction pattern caused by the sound field in the crystal. The observed complicated light picture is a composition of the diffraction responses from sound beams propagating in different directions inside the crystal. Some of these beams can be revealed easily: they are marked in the picture as true. There is also a mark that looks like the image of a sound beam ("False mark") but it is not such one. Presence of this mark cannot be explained simply from a study of the picture itself. In the course of the experiment, however, one could observe its delayed appearance and disappearance when the applied CW signal was switched on and off. It says that this light spot was not caused by a sound beam directly. Apparently, its appearance is caused by temperature phenomena connected with presence of sound waves. It is worth noting that all the three represented pictures were taken with the crystal position deviated from the optical system axes by the angles $\theta_h = -2^\circ 30'$ and $\theta_v = -2^\circ$ (see Fig. 4.1.1 for definitions). In case of other deviation angles, other sound beams could be observed more distinctively.

The second picture (Fig. 4.2.2) shows the diffraction pattern when the PM signal is applied. One can see that the images of the sound beams marked as true remained at the same positions. Since the duty cycle of the applied PM signal is equal to 0.1 their observed brightness decreased considerably because of the reduced exposure time. This image gives a much clearer picture of the sound field in the crystal: only a few spots on the left hand bottom side of the crystal mark the sound beams; the centre-symmetrical spots above the crystal represent the same beams. The shine around the crystal is a stray lighting that can be easily identified from image in Fig. 4.2.3 with no signal applied: in both pictures, the shine form and distribution are practically identical.

The sound beam marks shown in Figs. 4.2.1 and 4.2.2 had been easily detectable in the experiment, but they did not represent neither emitted nor reflected beams. Indeed, their spatial orientation is far from the "right" directions $[110]$ and $[001]$, which in the picture are the horizontal and vertical directions respectively. Hence, they do not represent the "right beams" which are the subject of the studies.

The problem with finding the "right beams", as mentioned in previous section, is that an efficient photoelastic coefficient $p_{eff} = 0$ for configuration of the optical experiment shown in Fig. 4.1.1 *a* when the sound beam propagates along the $[110]$ direction and the light beam along the $[\bar{1}\bar{1}0]$ one. For our purpose however, this configuration is of a particular interest, since just in this case the slow shear wave reflection is observed in the

figuration is of a particular interest, since just in this case the slow shear wave reflection is observed in the plane of incidence. The efficient photo-elastic coefficient becomes non-zero if the crystal is rotated with respect to the light beam and can be calculated using approach developed in [22, §9]. It depends on direction and polarization of acoustic and light waves as follows:

$$p_{eff} = \Re \varphi_{ij} \alpha_i \beta_j \quad (4.2.1)$$

where an auxiliary second rank tensor $\varphi_{ij} = p_{ijkl} \kappa_k \gamma_l$ depends only on tensor of photo-elastic constants p_{ijkl} and the unit vectors of direction κ and polarization γ of the sound wave; unit vectors α and β in (4.2.1) determine polarization of incident and diffracted light waves respectively. An auxiliary factor \Re combines a number of other factors affecting the value of p_{eff} but depending on geometry of acousto-optic interaction weakly. Efficiency of acousto-optic interaction is determined by a figure of merit [14] $M_2 = n^6 p_{eff}^2 / \rho v^3$ which is usually related to that of fused quartz $M_{2fq} = 1.51 \cdot 10^{-15} \text{ s}^3/\text{kg}$; here n is the index of refraction. Typical related values M_{fq} for different materials are from 0.5 to 30 with some record values up to 800.

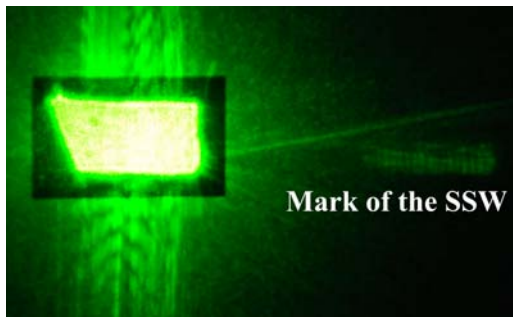


Fig. 4.2.4. Visualization of the SSW beam emitted by the transducer. *Polarization of the laser beam is vertical.* The CW signal is applied. Mark of the SSW is observable but is very vague because observation is made in the "forbidden" direction.

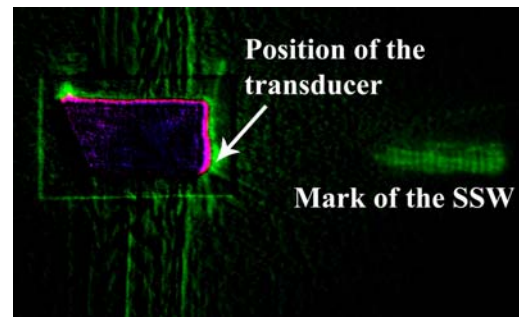


Fig. 4.2.5. Visualization of the SSW beam emitted by the transducer – the processed image obtained from the initial one presented in Fig. 4.2.4. Practically the whole path of the SSW along the [110] direction is visible.

The "right" SSW beam had been visualized with the crystal rotated by angles $\theta_v \approx 3^\circ 30'$ and $\theta_h \approx 3^\circ$ using an extraordinary polarized light beam corresponding to the vertically polarized one in Fig. 4.2.4. In this case, the calculated value $M_{2fq} = 7.8 \cdot 10^{-5}$ was very small. Nevertheless, we managed to visualize the SSW wave along the [110] direction but did not detect the reflected wave along [001]. The distinctive response from the SSW beam is presented in Fig. 4.2.5. This picture is the result of processing of the initially obtained photographs: the no-signal picture had been subtracted from the CW-signal picture presented in Fig. 4.2.4. The resulting picture was then added to itself to increase contrast and to improve the ultimate image. The transverse strips over the beam image are the light interference fringe caused by the crystal surfaces with no antireflection coatings. The vertical strips over the crystal image itself and the shine around its silhouette are the residual stray lighting not subtracted completely due to imperfect fixation of the camera in the experiments.

As seen from the obtained picture, the emitted beam propagates, as anticipated, along [110]. At the same time, unlike the case presented in Fig. 4.2.1, there are no responses from other sound beams that could represent a beam reflected towards the receiving transducer. There can be two evident reasons for that: (1) the stray light-

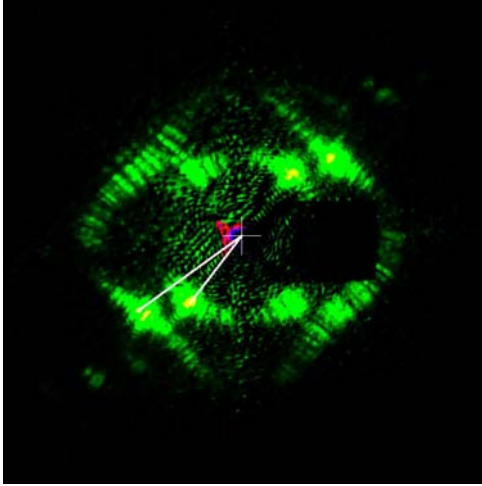


Fig. 4.2.6. Observation of the Schaefer-Bergmann's diffraction pattern. The CW signal is applied; the obtained picture is processed – the no-signal image is subtracted. Polarization of the laser beam is *horizontal*. The quasi-longitudinal and fast quasi-shear waves are observed.

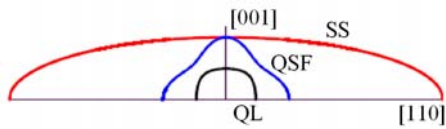


Fig. 4.2.7. The calculated slowness surfaces of sound waves propagating in the $(\bar{1}\bar{1}0)$ plane of TeO_2 . QL represents the quasi-longitudinal wave, QSF – the fast quasi-shear wave and SS – the slow shear wave.

As for the slow shear (SS) wave, no responses from it are observed in the obtained diffraction pattern. It means that in this experiment conditions to observe it were unsuitable.

Superimposition of the diffraction patterns obtained in the large- and small-aperture experiments enables to identify the sound beams of interest. This is demonstrated in Fig. 4.2.8 (see the next page) where the combined picture represents responses from the sound beams and the Schaefer-Bergmann's pattern simultaneously. One can see that spots from the QSF and QL waves identified in the Schaefer-Bergmann's pattern fall exactly on the sound beam images. Hence, the observed beams are formed just by these types of waves.

The spatial positions of the spots in the Schaefer-Bergmann's pattern give directions of the wave vectors \mathbf{K} with respect to the crystallographic axes of the crystal. Geometrical buildings in Fig. 4.2.9 (see the next page) show their polar angles θ_K . Calculated directions of the vectors of the group velocity are represented in the left upper corner of the picture as corresponding polar angles θ_s .

From the reported results, one can conclude that there exist much more wave beams in the crystal than that had been anticipated by the simplest physical model of plane waves underlying our analysis and the heuristic approach to designing the TIRUS body, which was developed in Section 1.2

ing, which is rather strong, masks a weak image of the reflected beam; (2) the conditions of the experiment are suitable to observe the only type of the sound wave, the slow shear wave along the $[110]$ direction. Both reasons are possible, but the latter looks more probable.

Identification of the types of the unanticipated "wrong" beams presented in Figs. 4.2.1 and 4.2.2 was done using sequential large- and small-aperture experiments. The Schaefer-Bergmann's diffraction pattern presented in Fig. 4.2.6 represents the result of the small-aperture experiment with a continuous wave signal. Directions of the white lines connecting the center of the picture and the light spots show directions of the slowness vectors or, what is the same, directions of the wave vectors of corresponding sound waves. To understand what type these waves are one ought to compare the diffraction pattern with calculated slowness surfaces presented in Fig. 4.2.7. As seen from Fig. 4.2.7 where they are presented, the shapes of the surfaces of the quasi-shear fast (QSF) and quasi-longitudinal (QL) waves are practically identical to the patterns observed in the experiment.

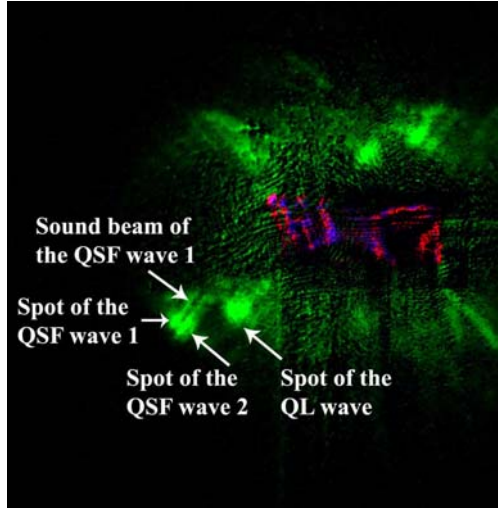


Fig. 4.2.8. Superimposition of the diffraction patterns obtained in the small- and the large-aperture experiments. The PM signal is applied; the obtained images are processed – the no-signal image is subtracted. *Polarization of the laser beam is horizontal.*

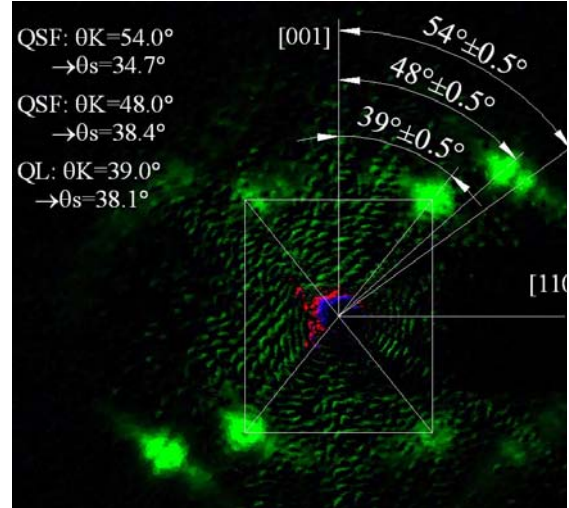


Fig. 4.2.9. Directions of the ray vectors of the observed wave derived from the directions of their wave vectors \mathbf{K} . θ_s and θ_K are corresponding polar angles. Two fast quasi-shear wave beams propagate at the angles $\theta_s \approx 34^\circ$ and $\theta_s \approx 38^\circ$. The quasi-longitudinal wave beam propagates at the angle $\theta_s \approx 38^\circ$.

5. Results and discussion

5.1 The sensor drawbacks

5.1.1 Mode conversions

Results of optical studies of the sound field in the sensor body show that the physical picture of the ultrasonic beam reflections in the crystal is more complicated than the model of the plane waves anticipates. Presence of quasi-shear and quasi-longitudinal waves, a lot of ultrasonic beams propagating in different directions – all this brings up the question of what could be a reason for the origin of these beams.

To answer this question let us analyze a typical waveform of the TIRUS output acquired from the oscilloscope (the blue channel in Fig. 5.1.1 on the next page) when the pulse modulated sine wave is applied to the emitting transducer (the yellow channel). The first pulse is delayed by $37.6 \mu\text{s}$ with respect to the applied one what is very close to the calculated delay time $\tau = \tau_{[110]} + \tau_{[001]} = 33.5 + 4 = 37.5$ (see Fig. 5.1.2 on the next page). In calculations, the velocity of the SSW along the [110] direction was taken 612.9 m/s , along the [001] direction – 2103.3 m/s). That is, the first pulse represents exactly the wave anticipated by the model put in the base of the TIRUS design. The fifth pulse is delayed by $\sim 76 \mu\text{s}$ with respect to the first one. It is approximately equal to 2τ , that is, the time needed for the sound pulse reflected from the receiving transducer to pass the round trip to the emitting transducer and, having been reflected, back to the receiving one. Thus, this fifth pulse also completely correlates with the scenario prescribed by the model used (see Section 1). Nothing like that can be said about pulses 2-4 because: firstly, they only appear *after* the moment when the first pulse appears, that is, *after reflection of the incident SSW from the reflecting plane*; secondly, from the above discussion we also know that there are exist the QSF as well as QL waves in the crystal. Therefore, it is reasonable to suppose that for no apparent

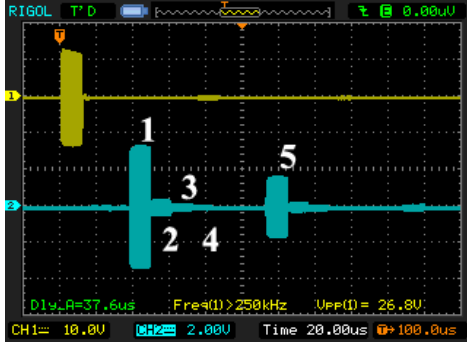


Fig. 5.1.1. Multiple responses at the TIRUS output (blue). A pulse modulated signal (yellow) is applied to the emitting transducer. 1 – the first delayed pulse; 5 – the "three pass" pulse produced by the SSW; 2-4 – pulses produced by waves which are the result of the incident SSW conversion into other types of waves, probably QSF and QL.

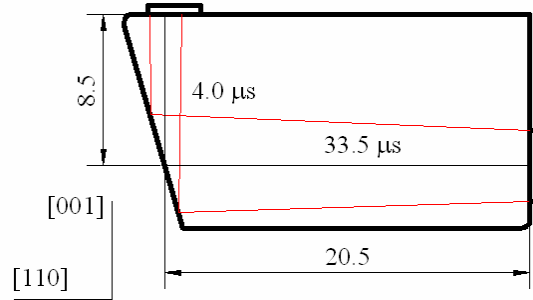


Fig. 5.1.2. Estimation of the delay time of the slow shear wave (SSW) in the crystal. The lengths of the SSW path along the [110] and [001] directions are given in mm. The emitting transducer is located on the right, the receiving one – on the top. The red lines show conditional boundaries of the sound beams.

reason conversion of the incident SSW into other types of waves takes place, probably into the QSF and QL waves detected by the receiving transducer.

As was discussed in Section 1.2.2, in the frame of the accepted model of plane waves there should be no mode conversions because the displacement vectors of all the plane wave components of the incident ultrasonic beam lie exactly in the reflecting plane. Recent studies [20, 23] show however that wave beams could not be considered as consisting of the plane waves exactly the same polarization. Perhaps such a reason can underlay mechanism leading to the wave mode conversions. One more reason could be the side lobes of the emitted sound beam in no way taken into account in the model used in the analysis. Another reason seems to be the ultrasonic beam divergence in the orthogonal plane (001) but calculations show it is the far-fetched one. Indeed, as seen from the sketch in Fig. 5.1.3, in the vicinity of the [110] direction, the displacement vector directions are almost the same even though the directions of the wave vectors change a little bit. Therefore they are still stay in the reflecting plane. Thus, for the time being no single well-grounded reason for excitation of other types of waves can be called. Although search for an actual reason of the observed phenomena is of a great interest, it was far out of the scope of the current project.

Whatever the reason, the discussed conversions evidently take place and might well have been the reason for the observed increase of the insertion loss of the TIRUS in the two-port-network experiments. Answering the question whether it was the main reason and a single one required further investigations.



Fig. 5.1.3. Polarization of the divergent slow shear wave beam propagating in plane (001) of TeO_2 .

As a matter of fact, the unexpectedly great value of the TIRUS insertion loss was not a drawback in the current studies because its value of ~10-15 dB did not prevent from getting reliable results. As it was reported in Section 3.1, the real obstacle was instability of the TIRUS complex transmission coefficient T including its phase shift

(see equation 3.1.1). Finding a real reason for that was not a subject of this project, nevertheless an estimation of possible temperature influence on the observed instability has been done.

5.1.2 Temperature instability

The temperature coefficients for the elastic constants of TeO₂ given in [6] were used as initial data. Paratellurite has strong anisotropy of all temperature coefficients, but for the types of elastic waves used in the TIRUS, the essential elastic constants affecting their velocities are c_{44} for shear wave along [001] and c_{11} and c_{12} for slow shear wave along [110]. Although all temperature coefficients for components c_{ij} of the stiffness tensor are negative, the one for the efficient constant $(c_{11}-c_{12})/2$ that determines the SSW velocity is positive and of the value $389 \cdot 10^{-6} \text{K}^{-1}$, which is much greater than corresponding coefficient for component c_{44} which is equal to $-73 \cdot 10^{-6} \text{K}^{-1}$. The same holds for the thermal expansion coefficients: the one for [110] ($20 \cdot 10^{-6} \text{K}^{-1}$) is almost three times greater the one for [001] ($6.6 \cdot 10^{-6} \text{K}^{-1}$). Both these factors lead to a significant difference between temperature coefficients γ of the sound wave velocities along the [110] and [001] directions which in the linear approximation can be determined as

$$\gamma = (\beta + \Sigma \alpha_i) / 2, \quad (5.1.1)$$

where β is a corresponding temperature coefficient of the efficient elastic constant and $\Sigma \alpha_i$ is the sum of the thermal expansion coefficients along the crystallographic coordinates. From this equation the following calculated temperature coefficients for the sound waves of interest are: $\gamma_{110} = 211 \cdot 10^{-6} \text{K}^{-1}$ и $\gamma_{001} = -13 \cdot 10^{-6} \text{K}^{-1}$.

An additional phase shift at the TIRUS output $\Delta\varphi$ due to both thermal effects, change of the sound velocity and the thermal expansion, can be calculated as

$$\Delta\varphi = 2\pi f \left(\frac{L_{110}^0}{v_{110}^0} - \frac{L_{110}^T}{v_{110}^T} \right) + 2\pi f \left(\frac{L_{001}^0}{v_{001}^0} - \frac{L_{001}^T}{v_{001}^T} \right), \quad (5.1.2)$$

where L and v with the subscript and superscript indices are the path length passed by the sound wave and its velocity along [110] and [001] directions respectively. An estimation of how both members contribute into the total phase shift shows that the contribution of the second member compared to the first one is by 100 times less and can be neglected. Then

$$\Delta\varphi \approx 2\pi f (\gamma_{110} - \alpha_{110}) \frac{L_{110}^0}{v_{110}^0} \quad (5.1.3)$$

and is, taking into account the path length along the [110] direction $L_{110} \approx 20$ mm, approximately equal to 57°K^{-1} at frequency $f=27$ MHz.

A typical change of the TIRUS insertion phase in time observed in the continuous wave experiments described in Section 3.1 is $\sim 80^\circ$ in 30 min that corresponds to the calculated temperature change $\sim 1.5^\circ \text{C}$. Under circumstances when there was no control of the external temperature in the experiments, this value looks reasonable to conclude that observed instability was apparently caused by dependence of the sound wave velocity on temperature.

5.2 Results of the tested objects examination

5.2.1 Tested objects

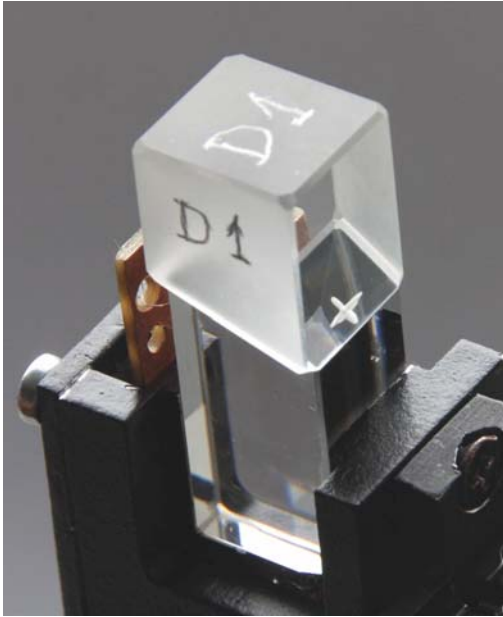


Fig. 5.2.1. The assembly "TIRUS-OUT" used in experiments with a defective Object Under Test.

An experimental proof of the TIRUS concept included necessarily experiments with tested objects, both flawless and defective ones. A comparative analysis of the obtained results was to answer the question whether the concept is proven or not.

In experiments, experimental tested objects were specimens of fused quartz with a polished surface, which could be attached to a working surface of the sensor using a technology of an optical contact. This technology provides an excellent acoustic contact [24] that makes the assemblies "TIRUS-OUT" be experimental samples with an almost ideal physical interface between the sensor body and a tested object. Here "OUT" stands for the Object Under Test. A typical example of such an assembly is shown in Fig. 5.2.1. Here the defective object #1 (on top) is bonded with the sensor (the crystal underneath) and

makes an assembly for investigations of the ultrasonic beam reflection in the sensor body. A defect on the surface of the tested object can be observed as a "crest" in the zone where the probing ultrasonic beam strikes the interface. The appearance of all flawless and defective tested objects examined in the experiments is presented in Fig. 5.2.2 and 5.2.3 respectively. Artificial defects were differently oriented cruciform scratches on their surfaces.

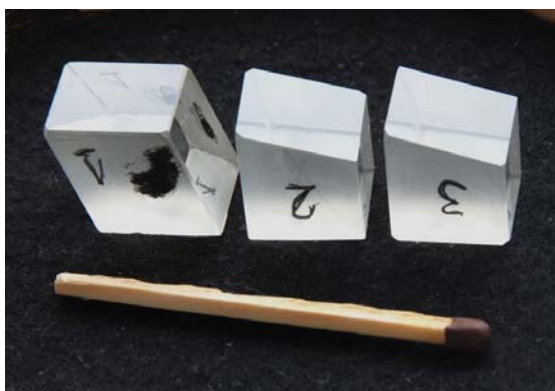


Fig. 5.2.2. Flawless specimens used in the experiments.

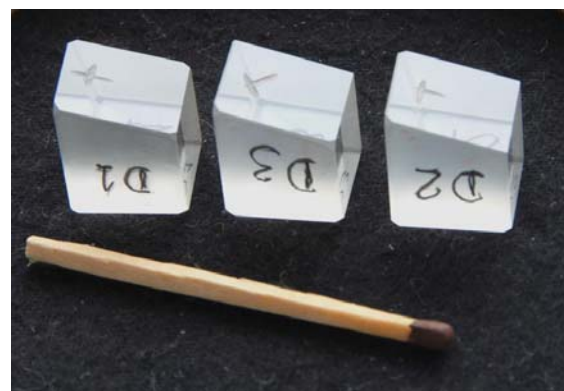


Fig. 5.2.3. Defective specimens with a single defect.

5.2.2 Results of the continuous wave experiments

As shown in Section 3.1, a frequency-shift-like instability of the TIRUS characteristics as a two-port network required application of the FFT to the acquired data to get a reference to which results of all other experiments could be compared. Therefore, all data obtained from the continuous wave experiments with both flawless and defective specimens were subjected to the same post-processing as data obtained from the TIRUS itself. All processed data on the TIRUS insertion phase turned out to lie within the 95% confidence interval of the TIRUS characteristic instability, that is, this characteristic provided no information that could be extracted from

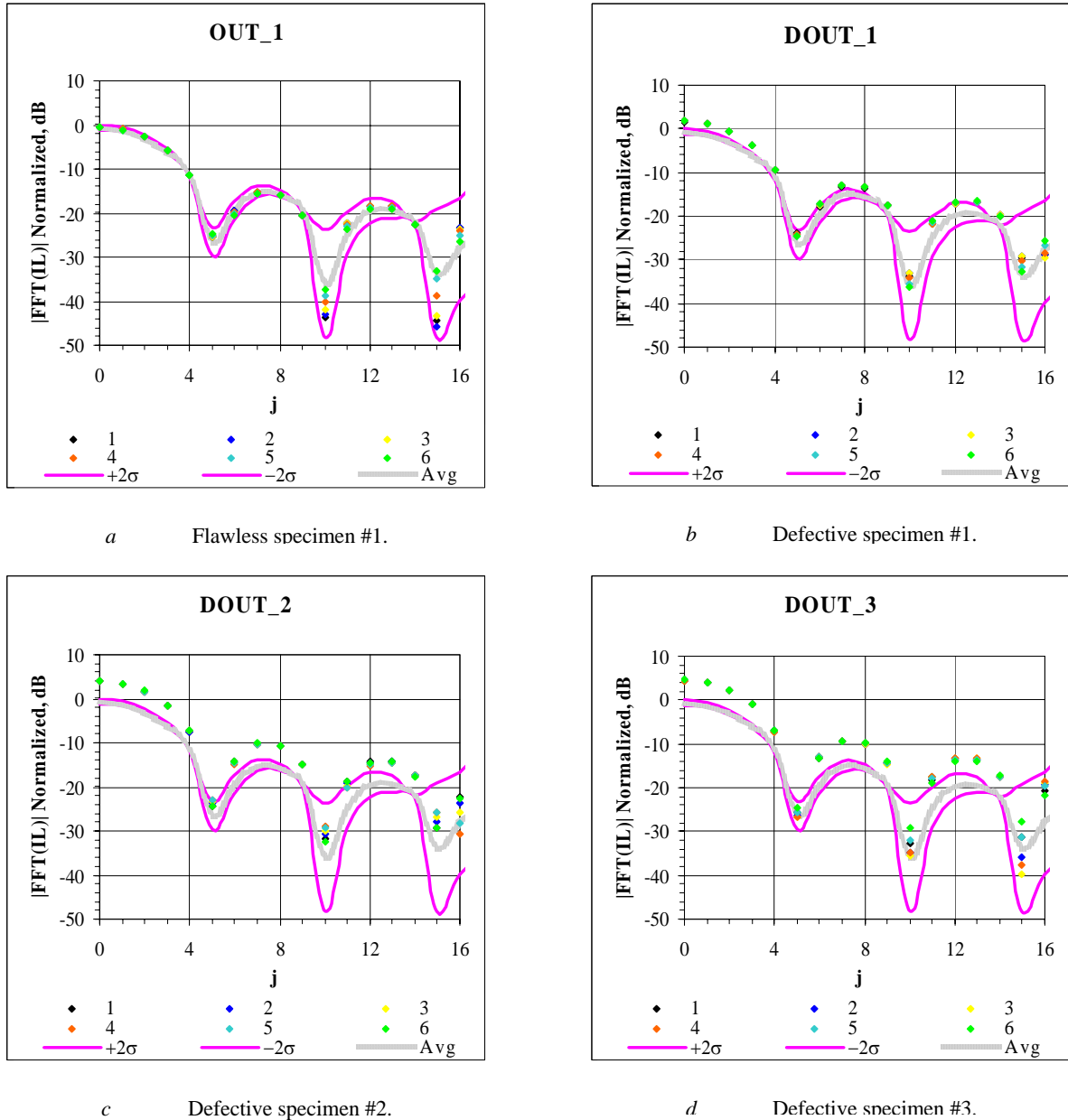


Fig. 5.2.4. Results of the continuous wave experiments with different tested specimens: comparison with the reference data. First 16 FFT coefficients are displayed of the insertion loss of the TIRUS contacting with the specimens. Numbers 1-6 correspond to the sequential measurements made at different moments of time: $t=0, +2, +4, +8, +16$ and $+32$ min. $\pm 2\sigma$ represents a 95% confidence interval. As seen from Fig. *a*, all FFT coefficients for the flawless object lie within the confidence interval while a number of FFT coefficients of all defective objects are out of it (Fig. *b-d*).

the phase change caused by the instability. For this reason, results of these measurements are not presented in the current report. At the same time, FFT of the TIRUS insertion loss IL gave very distinctive results, which allow one to discriminate reliably between flawless and defective specimens. In all experiments without exclusion, a qualitative difference between the results obtained with flawless and defective specimens were significant: for the former first 16 FFT coefficients lay within the confidence interval of the TIRUS own instability; for the latter these coefficients were mainly out of it except a few ones (the 5th, 10th and 15th) within it. The same tendency was observed in the repeated experiments with the same specimens although quantitative values of the FFT coefficients varied. This, though, can be explained by variations in the position of the defect with respect to the insonification area on the sensor working face in the repetitive experiments. Some of the results illustrating observed difference between the TIRUS response to flawless and defective specimens are presented in Fig. 5.2.4. The numbers 1-6 in the figure denote every single measurement in the series of measurements separated by a time interval. **Explicit difference in the TIRUS responses to flawless and defective objects under test proves feasibility of the proposed technique investigated in the frame of this project.**

5.2.3 Results of the experiments with time-gated signals

In the experiments with the time-gated signals an explicit instability of the TIRUS own transmission coefficient T_{TG0} , unlike the continuous wave experiment, could not be observed directly from the waveform read out from the oscilloscope. Instead, it was produced from the series of measurements and was expressed as a *reference value* of $T_{TG0}=0.327\pm 0.027$ to which all other results were compared. Here the parameter defining the 95% confidence interval is the value $2\sigma=0.027$ put into the reference value as the measurement error.

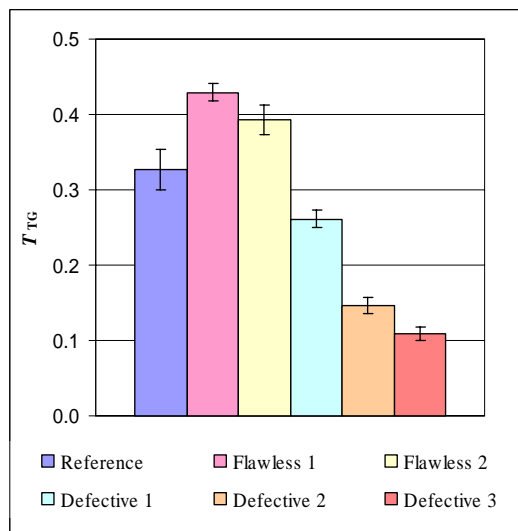


Fig. 5.2.5. Time-gated transmission coefficient of the TIRUS measured with different tested specimens. The displayed error bars corresponds to the 95% confidence interval.

The results of the measurements of the time-gated transmission coefficients T_{TG} for all specimens, both flawless and defective ones, are presented in Fig. 5.2.5. They demonstrate *an unexpected and strange effect absolutely inexplicable at a glance*: the reference transmission coefficient T_{TG0} is less than that measured in case of flawless specimens being in a contact with the working surface of the sensor. This effect, however, can have a simple explanation: presence of a flawless object changes boundary conditions on the reflecting plane and partly suppresses conversion of the incident slow shear wave into other types of wave. At the same time, the total internal reflection is not frustrated and no energy of the incident wave penetrates into the tested object. As a result, more its energy is reflected from the interface and the TIRUS

transmission coefficient increases. Another effect, the observed considerable difference between responses from two flawless specimens themselves, which theoretically should be negligibly small, can be caused by different reasons: by a residual stress after the applied optical contacting procedure, or by different roughness of tested surfaces, or different temperature conditions, or their combined influence. Whether all these effects actually take

place can be clarified only in further experiments which could not be conducted in the frame of the current project.

In case of defective specimens, all measured transmission coefficients are significantly less than the reference one. The important point here is that flawless and defective specimens affect the TIRUS transmission coefficient in different ways, either increasing or decreasing it. **That shows a specific response of the TIRUS to the presence of a defect. Thus, the obtained results, as well as the results obtained in the continuous wave experiments, prove feasibility of the Total Internal Reflection Ultrasonic Sensor.**

Conclusions

A heuristic model based on the theory of the plane elastic waves in crystals and calculations of the near field (Fresnel's) zone of the emitting transducer has been built and applied to development of a software simulating propagation and reflection of ultrasonic beams in plane (110) of TeO_2 . The developed software was applied to designing of an experimental sample of the Total Internal Reflection Ultrasonic Sensor (TIRUS) which then was fabricated and investigated as a two-port network using two types of 27 MHz driving signals, continuous wave (CW) and pulse modulated (PM) ones. Despite a significant instability of its transmission coefficient, the reference data were obtained using a specially developed procedure based of the FFT applied to the frequency response of the TIRUS insertion loss and phase.

An optical visualization of the ultrasonic field structure in the TIRUS body discovered unexpected ultrasonic beams of quasi-shear fast and quasi-longitudinal waves propagating in the crystal. A physical mechanism of their generation stays unclear because in the frame of the built up model they should not have been produced by the slow shear wave (SSW) reflection from the specifically oriented sensitive plane of the TIRUS. An analysis of experimental data shows however, that mode conversions at reflection seem really to take place and can produce the observed beams.

Experiments with specially fabricated specimens of fused quartz, both flawless and defective ones, were aimed at revealing a measurable effect caused by a defect on a surface of the defective specimens. The quantities measured were the magnitude and phase of the TIRUS transmission coefficient, which represented the magnitude and phase of the SSW reflected from the interface between the TIRUS body and an object under test. Phase measurements produced rather equivocal data, whereas amplitude measurements were productive: results of experiments with different specimens using either CW or PM signals showed a distinctive difference between the TIRUS responses to flawless or defective tested objects. This proves feasibility of the proposed concept and the developed technique.

Once the TIRUS concept is proved and the current project shows the ways in which such a sensor can be built, its results becomes a platform from which further research and development of the novel class of ultrasonic devices for detecting the subsurface flaws can be started.

Prospects

The main purpose of the project, proof of the concept of the TIRUS is achieved, but the accomplished research discovered some unanticipated problems and brought up the questions of:

- What a more adequate theoretical model could be developed instead of the heuristic one used in the project to describe reflection of ultrasonic beams in a strongly anisotropic crystal of a limited size?
- What is the actual reason of the observed mode conversions of ultrasonic waves? What is an impact of these conversions on the TIRUS properties?
- Is the temperature dependence of the sound velocity in TeO_2 the only reason for the observed instability of the TIRUS transmission coefficient? Can it be reduced by means of a specific crystal cut choice or be excluded by post-processing of measured signals?

Answering these questions requires rather different approaches and types of further investigations: the first one includes building a new theoretical model and corresponding calculations; the second implies thorough experimental investigations focused on the ultrasonic beam behavior and mode conversions; the third should combine temperature-controllable experiments, and choice and application of adequate signal processing techniques.

Further research aimed at reducing acquired knowledge to practice should apparently include not only all these mutually connected fundamental investigations but also more technical ones, such as examination of different types of tested objects and influence of the couplant on TIRUS capabilities, to find limitations of the proven concept.

References

- 1 G. A. Matzkanin, H. T. Yolken, TechSolutions 6: Selecting a Nondestructive Testing Method, Part V - Ultrasonic Testing. In AMMTIAC Quarterly, Vol. 2, No. 3 - Testing Materials in Different Microclimates (Published 2008-02-20). <http://ammtiac.alionscience.com/quarterly>
- 2 D. Royer, E. Dieulesaint, *Elastic Waves in Solids* v. 1, Springer-Verlag, Berlin Heidelberg New York, 2000, 374 p.
- 3 Fedorov, F. I. *Theory of Elastic Waves in Crystals*, Plenum Press, New York , 1968.
- 4 Cohen M. G., Optical Study of Ultrasonic Diffraction and Focusing in Anisotropic Media. J. Appl. Phys., v. 38, No. 10, p.3821-28 (1967).
- 5 M.A. Gnatyshyn, E.M. Smirnov, A.V. Yurchenko. Investigation of shear slow wave multiple reflection off free surfaces in paratellurite. Bulletin of the University of Kiev. Series: Physics & Mathematics. (In Ukrainian), No. 1, p. 230-233, (2007).
- 6 Y. Ohmachi, N. Uchida, Temperature Dependence of Elastic, Dielectric, and Piezoelectric Constants in TeO₂ Single Crystals. J. Appl. Phys., v. 41, No. 6, p.2307-11, (1970).
- 7 L. P. Voitenko, E. M. Smirnov, A. V. Yurchenko. Direct Observation of Slow Shear Wave Reflection in the Plane (110) of Paratellurite. Bulletin of the University of Kiev. Series: Radiophysics & Electronics. (In Ukrainian), No. 11, p.13-16, (2008).
- 8 Acoustic Properties of Solids, <http://www.ondacorp.com/images/Solids.pdf> .
- 9 L.M. Brekhovskikh, *Waves in Layered Media*. Moscow: Nauka, 1973 373 p. (In Russian. English translation: Brekhovskikh L.M., *Waves in Layered Media*. New York: Academic Press, 1960. 561 p.)
- 10 M. Spies, Ultrasonic Beam Field Modeling – Fundamentals and Applications in Nondestructive Evaluation. Proceedings of the World Congress on Ultrasonics WCU 2003, September 7-10, 2003, Paris, p.1521-28.
- 11 Y. Ohmachi, N. Uchida, N. Niizeki, Acoustic Wave Propagation in TeO₂ Single Crystal. JASA, v. 51 No. 1 (Part 2), p. 164-8, (1972).
- 12 A.V. Yurchenko Presentation of a loaded piezo-plate with a simplified equivalent circuit. Izvestiya VUZ, Radioelektronika, 1981, No. 3, p. 74-8. (In Russian – translated into English by Allerton Press, Inc as Radioelectronics and Communications Systems).
- 13 E. G. Spencer, P. V. Lenzo, A. A. Ballman, Dielectric Materials for Electrooptic, Elastooptic, and Ultrasonic Device Applications. Proceedings of the IEEE, v. 55, No. 12, p. 2074-104, 1967.
- 14 D. Royer, E. Dieulesaint, *Elastic Waves in Solids II. Generation, Acousto-optic Interaction, Applications*. Springer-Verlag, Berlin Heidelberg New York, 2000, 446 p.
- 15 R. Truell, Ch. Elbaum, B. Chick, *Ultrasonics Methods in Solid State Physics*. (Russian translation), Moscow, "Mir", 1972.
- 16 A. Penttinen and M. Luukkala, Diffraction losses associated with curved ultrasonic transducers. J. Phys. D: Appl. Phys., Vol. 10, p. 665-9, 1977.
- 17 V. V. Galanin and V. S. Kononenko, The Influence of the Electrode Diameter on the Diffraction Effects in the Ultrasonic Field Generated by an Oscillating Piezoelectric Disk. Acoustical Physics, Vol. 51, No. 4, 2005, pp. 392–6.
- 18 D. J. Hudson, *Statistics for Physicists*. (Russian translation), Moscow: Mir, 1970, 296 p.
- 19 Methods of Experimental Physics, vol. 1 – Classical Methods. Plenum Press Inc., New York , 1959.
- 20 V. N. Parygin, A. V. Vershubskii, Yu. G. Rezvov, Acoustooptic interaction of beams close to forbidden directions. Optics and Spectroscopy, vol. 90, No. 1, 2001, pp. 129–135. (Translated from Optika i Spektroskopiya, Vol. 90, No. 1, 2001, pp. 144–151).
- 21 L. Bergmann, *Ultrasound and Its Application in Science and Engineering*. (Russian translation), IL, Moscow 1957.

22 I. L. Fabelinskii *Molecular scattering of light*. Moscow: Nauka, 1965, p. 512. (In Russian). (English: Molecular scattering of light, by Immanuel L. Fabelinskii. Translated from Russian by Robert T. Beyer. New York, Plenum Press, 1968, 622 p.).

23 Yu. S. Dobrolenskiy, V. B. Voloshinov, and V. N. Parygin, Collinear diffraction of a divergent light beam by ultrasound in a paratellurite crystal. *Optics and Spectroscopy*, Vol. 98, No. 4, 2005, pp. 618–623. (Translated from *Optika i Spektroskopiya*, Vol. 98, No. 4, 2005, pp. 673–678).

24 Research on Optical Contact Bonding. Final rept. 15 May 1963-30 May 1966, Corporate Author: DEVICE DEVELOPMENT CORP WALTHAM MA. Personal Authors: Holt R. B. ; Smith H. I. ; Gussenhoven M. S. <http://www.dtic.mil/cgi-bin/GetTRDoc?AD=AD643285&Location=U2&doc=GetTRDoc.pdf>



Oleksandr Yurchenko

Project manager